INTRAOPERATIVE LABEL-FREE MULTIMODAL NONLINEAR OPTICAL IMAGING OF TUMOR MICROENVIRONMENTS AND EXTRACELLULAR VESICLES

BY

YI SUN

THESIS

Submitted in partial fulfillment of the requirements
for the degree of Master of Science in Electrical and Computer Engineering
in the Graduate College of the
University of Illinois at Urbana-Champaign, 2017

Urbana, Illinois

Adviser:

Professor Stephen A. Boppart

Abstract

In recent years, various label-free nonlinear optical imaging techniques have been developed and applied in biomedical fields to provide unique imaging contrasts to biological tissues and act as promising noninvasive diagnostic tools in clinical tasks, like tumor margin determination. Especially, thanks to the advance of high-powered ultrafast pulsed lasers, integration and simultaneous acquisition of multiple nonlinear optical imaging modalities based on a single laser source have been made possible in the lab to generate real-time multi-contrast images of the *ex vivo* tumor microenvironment. While this simultaneous multimodal imaging system can acquire images that give insight into the tumor microenvironment, the lab-based nature restrains its application for more clinical studies because of the limited access to untreated fresh human tissue. This thesis reports the design, intraoperative operation, and promising results of a portable label-free multimodal nonlinear optical imaging system. By imaging untreated human breast tumor tissue immediately after surgical excision, the tumor microenvironment was visualized with high fidelity. The breast tumor subtypes as well as subtle tissue changes and activities such as desmoplastic reaction and apocrine metaplasia were recognized and validated by comparing with histology. In particular, tumor-associated extracellular vesicles (EVs), recently found to play essential roles in tumor progression, were identified and characterized in intraoperative multimodal nonlinear optical images before they experience any degradation, which is usually the case for human tissue imaged by lab-based multimodal nonlinear optical imaging systems due to tissue transportation. Quantification of EVs using intraoperative image data correlated well with pathological diagnoses like cancer invasiveness grade and closest tumor distance. This unique method of EV visualization provides new insights into tumor invasion in the microenvironment and may help achieve an innovative approach to cancer invasiveness determination and tumor margin assessment.

Acknowledgments

I would like to first thank Professor Stephen Boppart for his ideas of clinical translation of this novel imaging technique, and continued support throughout this work. This project has been a challenge as well as a precious experience for me to get familiar with the big "playground" in the Biophotonics Imaging Laboratory (BIL).

I would also like to thank Dr. Haohua Tu for his optics expertise and advice that initiate the work in this thesis; and I would like to thank Dr. Marina Marjanovic and Eric Chaney for their biological and medical knowledge and experience, as well as Sixian You and Darold Spillman for the technical help with both hardware and software, without which the intraoperative imaging system could not have been finished. Especially, I would like to acknowledge the help and advice from Dr. Zheng George Liu, Dr. Anna Higham, Dr. Kimberly Cradock, Janet Iverson and other collaborating doctors and staff members at Carle Foundation Hospital, who contributed to this intraoperative research and provided all the support.

Finally, I would like to thank my parents as well as my best friend, Zhengzheng, for supporting and encouraging me from the other end of this planet.

Contents

1 Introduction and background

Nonlinear optical imaging was developed and has emerged as a powerful tool for biomedical study in the past few decades. The high-intensity nonlinear optical interactions assure intrinsic optical tissue sectioning without the use of a physical pinhole as in confocal microscopy [1]. More importantly, these nonlinear imaging modalities, including two-photon fluorescence (2PF) and second harmonic generation (SHG), can provide unique molecular and structural contrast that can effectively and faithfully visualize various features like the distribution of flavin adenine dinucleotide (FAD) [2] and collagen fibers [3], respectively. These endogenous nonlinear optical contrasts enabled *ex vivo* and *in vivo* imaging of biological tissues that provide vital information of biological and clinical interest.

While each individual nonlinear imaging modality possesses its own specialty in biological studies, integration of multiple modalities benefits even more [4]. Multimodal nonlinear optical imaging systems developed in recent years have acquired co-registered multi-contrast images from different imaging modalities, which respectively highlight certain biological features. When combined, these features were found to be tightly connected and yielded high-dimensional information that gave more insight than simply adding modalities together [4,5]. For instance, the presence of cells by 2PF and surrounding collagen fiber alignment by SHG can be used to determine cell types and malignancy by combinatorial analysis [6].

However, most lab-based nonlinear optical imaging systems still use animal models in cancer studies, which are generally of less significance than studies involving human subjects. Although it is possible to image excised human breast tumor tissue in the lab, the collected image data are usually perturbed and distorted by surgical dyes and other artifacts induced during tissue preservation. Specifically, vulnerable structures such as extracellular vesicles (EVs) are liable to lose structural or functional fidelity, or even completely decompose after several hours. Therefore, human EV information acquired using a lab-based imaging system can often be problematic, and inaccurately represent the properties of EVs found *in vivo*.

There are currently several studies focusing on using nonlinear optical imaging intraoperatively for clinical and especially diagnostic applications. Raman-based imaging techniques like stimulated Raman scattering (SRS) are utilized in intraoperative imaging [7]. By exciting and manipulating several Raman-bands around the CH spectral region, cell nuclei, as the most commonly used biomarker in pathology, are clearly highlighted in processed images, which, after rescaling a colormap, highly resemble the conventional hematoxylin and eosin (H&E)-stained histology. A blind survey done by pathologists using these SRS images revealed high diagnostic precision [7]. An alternative approach introduced the use of fluorescent dyes to highlight nuclei and collagen fibers at video rate, but severely perturbed the tumor microenvironments [8]. These approaches to develop intraoperative nonlinear optical imaging systems are all focused on tissue anatomy and imitating H&E-stained histology. Few efforts have been devoted to imaging tumor microenvironments, which include nano-to-microscale structures like EVs and their distributions in and around tumors and seemingly normal tissues. Specifically, studies of EVs revealed the fact that EVs start working as messengers to transfer molecular information for tumor progression even before any cancer-related anatomical features emerge [5]. Visualization and analysis of tumor microenvironments would contribute to a better understanding of the underlying mechanism of cancer invasion. In addition, there is enormous potential to develop EVs as a new biomarker that can diagnose cancer at an earlier stage.

1.1 Nonlinear optical imaging modalities

Based on intrinsic optical signatures of biological structures, four nonlinear optical imaging modalities are integrated with a single light source and completely decoupled multichannel detection. Label-free multiphoton imaging modalities make use of nonlinear optical processes that can be induced in biological tissue including second harmonic generation (SHG), third harmonic generation (THG), two-photon fluorescence (2PF), and three-photon fluorescence (3PF), all of which can be demonstrated through derivation of the nonlinear electric polarization $\tilde{P}^{NL}(t)$.

One can start from a simplified expression of the electrical field of the incident laser beam in the temporal domain:

$$\begin{aligned}\mathcal{E}(t) &= \mathrm{Re}\{E(\omega)\exp(j\omega t)\} \\ &= \frac{1}{2}[E(\omega)\exp(-j\omega t) + E^{*}(\omega)\exp(j\omega t)],\end{aligned} \tag{1.1}$$

where $E(\omega)$ is the electrical field amplitude oscillating at angular frequency ω. To be noticed, the temporal electric field $\mathcal{E}(t)$ contains $E(\omega)\exp(-j\omega t)$ along with its complex conjugate to obtain the real-valued electrical field that exists in practice. Then, the electric polarization induced by this incident laser beam in a sample material (assuming the material is dispersionless and lossless) is calculated as:

$$\begin{aligned}\tilde{P}(t) &= \epsilon_0[\chi^{(1)}\tilde{\mathcal{E}}(t) + \chi^{(2)}\tilde{\mathcal{E}}^{2}(t) + \chi^{(3)}\tilde{\mathcal{E}}^{3}(t) + \chi^{(4)}\tilde{\mathcal{E}}^{4}(t) + \chi^{(5)}\tilde{\mathcal{E}}^{5}(t) + \cdots] \\ &\equiv \tilde{P}^{(1)}(t) + \tilde{P}^{(2)}(t) + \tilde{P}^{(3)}(t) + \tilde{P}^{(4)}(t) + \tilde{P}^{(5)}(t) + \cdots,\end{aligned} \tag{1.2}$$

where $\tilde{P}^{(1)}(t)$ represents the linear electric polarization, and $\tilde{P}^{(2)}(t)$ with other higher-order terms are nonlinear electric polarizations at second order and higher. Among these nonlinear electric polarizations, SHG can be explained by the second-order $\tilde{P}^{(2)}(t)$, while THG and 2PF are contained in $\tilde{P}^{(3)}(t)$, and 3PF is from $\tilde{P}^{(5)}(t)$.

Although every order of nonlinear electric polarization is included in Eqn. (1.2), there are some of them absent in certain types of media. For instance, due to its quadratic dependence on the electric field, $\tilde{P}^{(2)}(t)$ vanishes in centrosymmetric media, which enables SHG, a special second-order nonlinear optical process, to depict tissue structure lacking centrosymmetry. There are many characteristics of these nonlinear processes that act as advantages for microscopy. For example, because the nonlinear polarizations of material depend on higher orders of the incident electric field, nonlinear optical signal generation is confined in a tighter region around the focal point where the electric field is sufficiently high. In addition, nonlinear electric susceptibilities are orders of magnitude smaller than the linear one, which means only the nonlinear signal generated near the focal point is large enough to be effectively

detected. These properties of nonlinear optical processes offer an alternative approach to optical sectioning, other than conventional confocal microscopy, and make it possible for nonlinear optical imaging to assess the three-dimensional (3D) microstructure in volumes of tissue, even *in vivo*.

1.1.1 Second harmonic generation

SHG is one of the most well-known nonlinear optical processes [9]. As a parametric nonlinear optical process, SHG is not involved with any form of energy transfer between matter and the electromagnetic field. In other words, there is no real energy state transition occurring in the material molecules interacting with SHG photons. Instead, as illustrated in the Jablonski diagram in Figure 1.1 the entire SHG process can be viewed as the two-photon excitation of a molecule to a virtual state with nearly no lifetime, followed by the instantaneous decay to its ground state, along with the generation of a photon with twice the incident photon frequency.

Being a second-order nonlinear process, SHG only exists in non-centrosymmetric media with non-zero $\chi^{(2)}$ susceptibility. Consider an incident laser beam with a simplified temporal expression of Eqn. (1.1) where the second-order polarization $\tilde{P}^{(2)}(t)$ is described as:

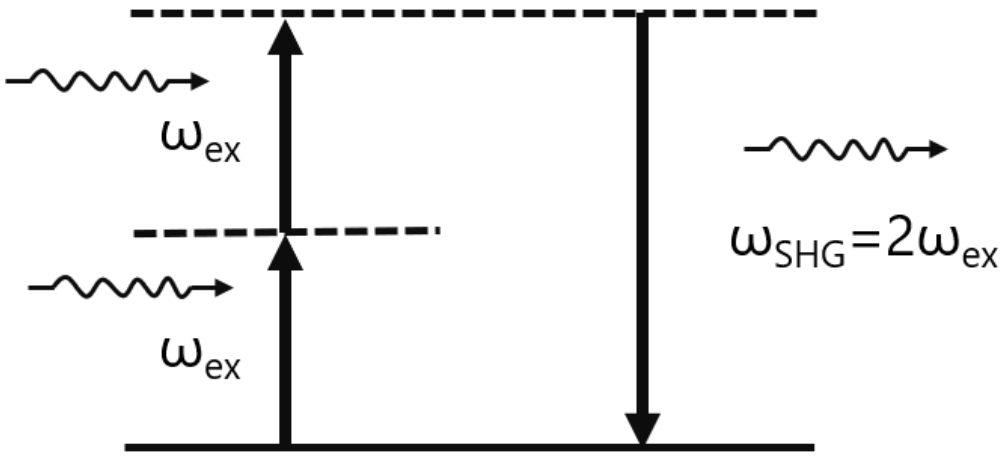

Figure 1.1 Jablonski diagram of SHG. The term ω_{ex} is the frequency of incident excitation photons, and $\omega_{SHG} = 2\omega_{ex}$ represents the frequency of the emitted photon generated from the SHG process.

$$\begin{aligned}\tilde{P}^{(2)}(t) &= P^{(2)}(0) + P^{(2)}(2\omega)\exp(-j2\omega t) + c.c. \\ &= \frac{1}{4}\epsilon_0\chi^{(2)} \mid E(\omega)\mid^2 + \frac{1}{4}\epsilon_0\chi^{(2)}E^2(\omega)\exp(-j2\omega t) + c.c.,\end{aligned} \tag{1.3}$$

where $P^{(2)}(0)$, with its complex conjugate in $c.c.$, are called optical rectification; $P^{(2)}(2\omega)$ and its complex conjugate in $c.c.$, oscillating at frequency 2ω and -2ω, represent SHG of the incident laser beam with oscillation frequency ω; and the $c.c.$ contains the complex conjugate of previous terms. In general, $\tilde{P}^{(2)}(\mathbf{r}, \mathrm{t})$ changes its sign with inverse spatial coordinate $\mathbf{r}$. However, in centrosymmetric media where $\chi^{(2)}$ shows inversion symmetry as $\chi^{(2)}(\mathbf{r}) = \chi^{(2)}(-\mathbf{r})$, because $\tilde{P}^{(2)}(\mathbf{r}, t)$ only contains quadratic components of the incident electric field, it is supposed to preserve its original sign with the sign of the spatial coordinate $\mathbf{r}$ being reversed. To satisfy both requirements, the only solution of $\tilde{P}^{(2)}(\mathbf{r}, t)$ is to vanish everywhere in centrosymmetric media.

Based on these unique properties, SHG is commonly applied in microscopy to visualize the $\chi^{(2)}$ response of a sample. In breast tumor and tissue imaging, the SHG signal is often generated from collagen fibers [10], whose density and alignment pattern can indicate the presence and aggressiveness of the tumor [11]. In label-free nonlinear optical imaging applications, collagen fiber structures visualized by SHG also act as a supplementary reference for tissue structure characterization [4].

1.1.2 Third harmonic generation

THG is a third-order nonlinear optical process. It involves three incident photons and generates a new photon with three times the original photon energy. Because THG is also a parametric optical process like SHG, there is no transition between real energy states, which is illustrated in Figure 1.2.

The nonlinear electric polarization of THG is also derived from Eqn. (1.1):

$$\begin{aligned}\tilde{P}^{(3)}(t) &= P^{(3)}(\omega)\exp\{-j\omega t\} + P^{(3)}(3\omega)\exp\{-j3\omega t\} + c.c. \\ &= \frac{3}{8}\epsilon_0\chi^{(3)} \mid E(\omega)\mid^2 E(\omega)\exp(-j\omega t) \\ &+ \frac{1}{8}\epsilon_0\chi^{(3)}E^3(\omega)\exp(-j3\omega t) + c.c.,\end{aligned} \tag{1.4}$$

where the first term and its complex conjugate represent the optical Kerr effect and two-photon absorption, and the second term along with its complex conjugate that oscillate at a frequency with absolute values three times as high as that of the incident electric field describe THG. Unlike SHG, this process exists in most media regardless of the centrosymmetric features. However, due to the smaller susceptibility $\chi^{(3)}$ and the more demanding phase matching requirement, THG signals are rarely observed in bulk materials with normal dispersion [12,13]. In response, studies using THG in applications found that significantly higher THG intensities are generated near material interfaces when using a tightly focused Gaussian beam for excitation [13,14] which can be attributed to the discontinuity in refractive index or nonlinear susceptibilities and the properties of a tightly focused Gaussian beam [13].

The advantages of THG have been utilized to investigate interfaces in biological tissues [4,15]. Using THG microscopy, adipocytes and lipid droplets can be easily visualized by the strong THG signal generated from their boundaries [4,15]. In addition, because of their membrane structures, EVs have also been characterized using the THG signal [5].

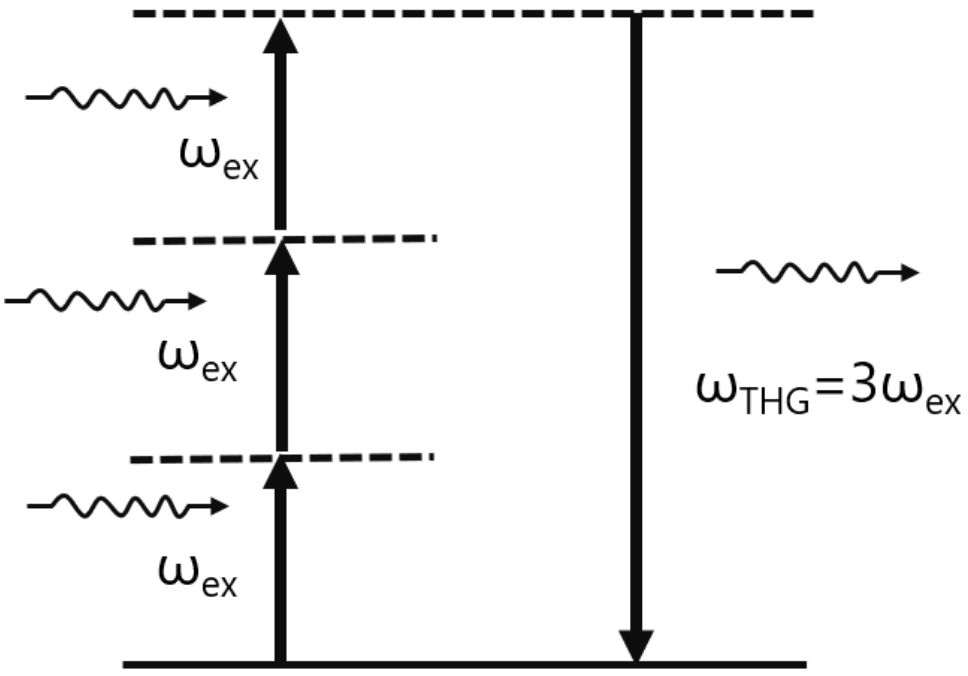

Figure 1.2 Jablonski diagram of THG. The term ω_{ex} is the frequency of the incident excitation photons and $\omega_{THG} = 3\omega_{ex}$ represents the frequency of the emitted photon generated by the THG process.

1.1.3 Two-photon fluorescence

Two-photon fluorescence is a widely used nonlinear imaging modality [16] that can probe endogenous fluorescence emitted from certain intrinsic fluorescent biomolecules. It can be understood as two major steps: two-photon absorption followed by fluorescence emission. Different from SHG and THG that only transfer molecular populations to virtual energy levels, two-photon absorption is a nonparametric nonlinear optical process that involves population transfer between real energy levels of molecules. The corresponding Jablonski diagram of 2PF is illustrated in Figure 1.3. First, the biomolecules, with the same energy state distribution as in Figure 1.3, are excited to a specific higher energy state among a group of energy states with the same principal quantum number through absorption of two identical incident photons. After a certain period of time known as the lifetime of this energy state, biomolecules relax to a lower molecular energy state via non-radiative decay (dashed arrows in Figure

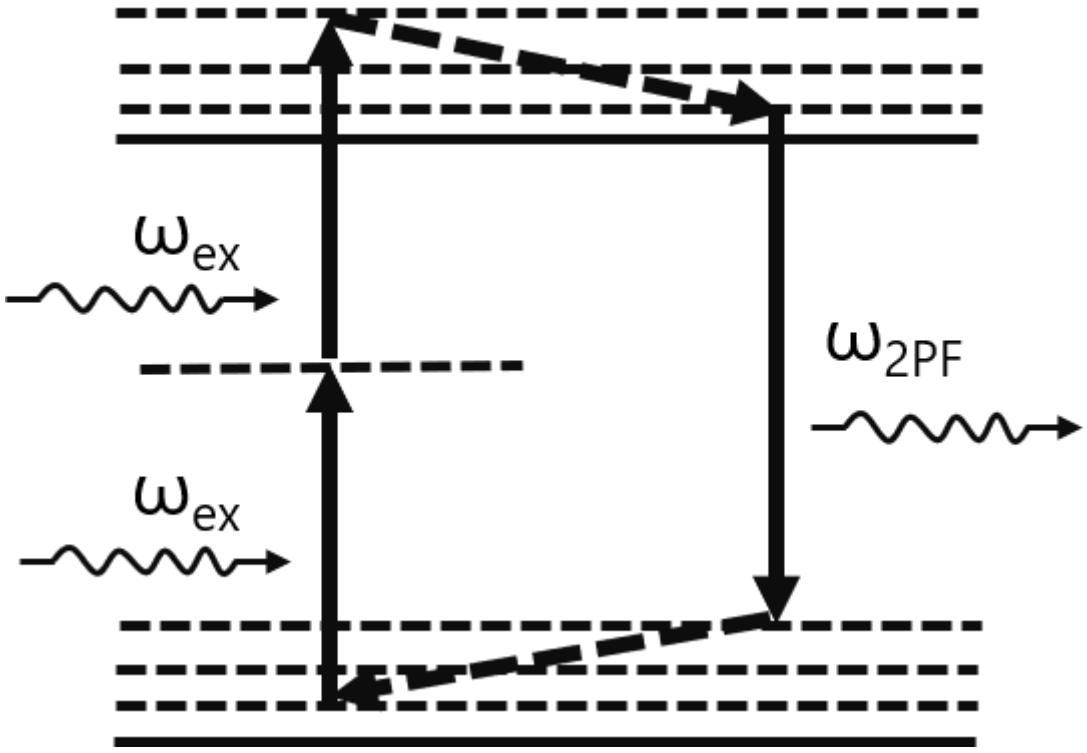

Figure 1.3 Jablonski diagram of 2PF. The term ω_{ex} is the frequency of the incident excitation photons and ω_{2PF} represents the frequency of the emitted photon generated by the 2PF process. Horizontal solid and dashed lines represent real energy states of the fluorescent molecules. Dashed arrows represent the process of nonradiative decay.

1.3). This lower energy state, unlike the state before non-radiative decay, is very unstable, and thus tends to readily decay to one of the ground states while emitting a fluorescent photon. Afterward, the biomolecules will experience another non-radiative decay and often fall back to the initial state that existed before the two-photon absorption event. There are special situations where a small portion of biomolecules, or fluorescent molecules that are used as labels, are trapped in one of the ground states and fail to reinitialize single- or multi-photon absorption. When collecting time-lapse image data, often an increasing number of fluorescent molecules will be trapped in these states, and the fluorescent signal will diminish, then finally vanish. This effect is known as photo-bleaching. Fortunately, compared to single-photon fluorescence, 2PF and other multiphoton fluorescence processes suffer much less from photo-bleaching. Because these nonlinear optical processes confine the excitation to a sub-femtolitre volume inside the sample, fluorophores from adjacent locations could quickly diffuse into the photo-bleached focal volume and help suppress the photo-bleaching effect [17].

It is obvious that 2PF is highly selective of biomolecules. Requirements for biomolecules that have a 2PF response include: an exact energy discrepancy between two molecular states, high probability of non-radiative decay, a fluorescent state, and a low chance of photo-bleaching. As a result, among the numerous kinds of biomolecules in human breast tissue, only a few of them can generate 2PF in response to near IR excitation wavelengths. Therefore, unlike SHG and THG that are sensitive only to tissue structures, 2PF and other multiphoton fluorescence processes can highlight molecular information such as the distribution and concentration of specific kinds of biomolecules.

As a special case of a third-order nonlinear optical process, the two-photon absorption process is represented by the first term of Eqn. (1.4), corresponding to the imaginary part of $\chi^{(3)}$. To calculate the absorption coefficient, the wave equation with nonlinear polarization $\tilde{P}^{(3)}(t)$ as a source term can be listed as:

$$\nabla^2\tilde{\mathcal{E}} - \frac{n^2}{c^2}\frac{\partial^2\tilde{\mathcal{E}}}{\partial^2 t} = \mu_0\frac{\partial^2\tilde{P}^{(3)}}{\partial^2 t}. \tag{1.5}$$

Considering the components of both sides of Eqn. (1.5) that oscillate at frequency ω and applying the slowly-varying-amplitude approximation, it can be derived from Eqn. (1.5) that

$$\frac{d}{dz}E(z)=\frac{3i\mu_0\omega c}{8n}\epsilon_0\chi^{(3)}\,|E(z)|^2\,E(z), \tag{1.6}$$

where *z* represents the location along the propagation direction. Substituting $E(z)$ with intensity $I(z)$ and considering the imaginary part of $\chi^{(3)}$, Eqn. (1.6) is derived as:

$$\frac{dI(z)}{dz}=-\frac{3\omega}{2n_0{}^2c^2\epsilon_0}\chi^{(3)}_{Im}I(z)^2=-\beta I(z)^2, \tag{1.7}$$

which yields the two-photon absorption coefficient β [18, 19].

In biological tissues, FAD is an important two-photon excited fluorophore whose concentration in cells has been used to study metabolic activity [20]. In particular, using label-free nonlinear optical imaging, exceptionally strong 2PF signal was found inside stromal cells in rat mammary tumor tissue and was even observed *in vivo* [4, 6]. This potentially indicates that high concentrations of FAD are contained in stromal cells [6]. In addition, elastin fibers are another source of 2PF [21] that have been found in our study to be especially dense in healthy breast tissues.

1.1.4 Three-photon fluorescence

Similar to 2PF, 3PF is also a fluorescent imaging modality [22, 23], but is initiated by three-photon absorption (Figure 1.4) and has a cubic dependence on incident light intensity. Similar to the calculation in Section 1.1.3, its absorption coefficient can be calculated from the fifth-order nonlinear electric polarization [19]

$$\gamma=\frac{5\omega}{2n_0{}^3c^3\epsilon_0^2}\chi^{(5)}_{Im}, \tag{1.8}$$

which when combined with one- and two-photon absorption coefficients, results in the optical absorption differential equation:

$$\frac{dI(z)}{dz}=-\alpha I(z)-\beta I(z)^2-\gamma I(z)^3. \tag{1.9}$$

Obviously, the intensity of 3PF is much weaker than 2PF due to the higher order nonlinearity. Furthermore, mode-locked Ti:sapphire lasers, as a conventional laser source for 2PF microscopy, can only generate 3PF in the spectral range from 200 to 300 nm, which would be strongly absorbed by tissues. Therefore, other pulsed laser sources with central wavelengths above 1000 nm have been investigated to generate 3PF signals that are less dependent to tissue absorption [4, 23]. Besides, using this excitation band also increases the multiphoton imaging depth because longer wavelengths are generally scattered less in biological tissues [23]. Another advantage of 3PF imaging is the high excitation localization that is intrinsically assured by higher-order optical nonlinearity [23].

By including 3PF in this multimodal nonlinear optical imaging system, the distribution of NADH, lipids, and other endogenous fluorophores in human breast tumor tissue can be visualized. Tissue features like endothelial cells and the inner contents of lipid droplets and adipocytes are highlighted by 3PF [6]. Because of the high excitation localization, 3PF also becomes a powerful tool for studying nanometer-sized structures like EVs [5].

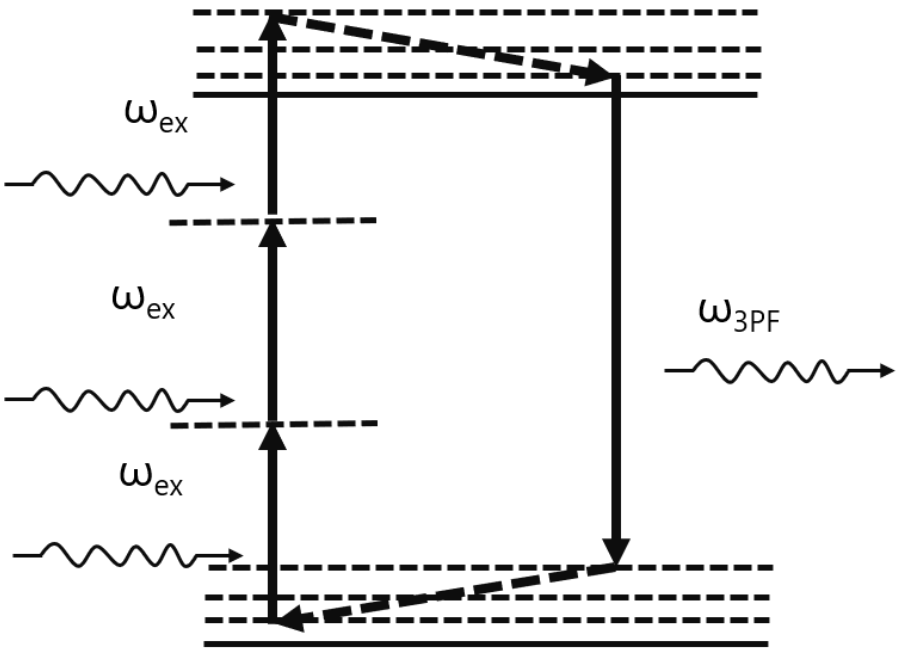

Figure 1.4 Jablonski diagram of 3PF. The term ω_{ex} is the frequency of the incident excitation photons and ω_{3PF} represents the frequency of the emitted photon generated by the 3PF process. Horizontal solid and dashed lines represent real energy states of the fluorescent molecules. Dashed arrows represent the process of nonradiative decay.

1.2 Ultrafast laser-scanning microscopy

There are various kinds of microscopes that can be classified in terms of their light delivery methods. Conventional bright field microscopes use lamps to illuminate the whole imaging field, which is then detected by a camera to create a wide-field absorbance image with no time delay. Absorption or a labeled fluorescence signal can be generated under this kind of microscope scheme. In general, high brightness of a lamp is not essentially required. However, as for label-free nonlinear optical imaging, generated signals are normally orders-of-magnitude weaker due to the small nonlinear optical cross sections of molecules and structures that exist intrinsically in biological tissue. Therefore, exceptionally high light intensity excitation is required to generate detectable label-free nonlinear optical signals.

One way of realizing high excitation intensity is to use femtosecond laser pulses, in which the photons are concentrated into ultrashort laser pulses that only occupy a small fraction of time. By doing so, ultrahigh optical peak intensity is realized for nonlinear optical interactions while maintaining a low average power to avoid potential laser damage. For instance, considering a pulsed laser with 80 MHz repetition rate, 100 fs pulse duration, and a moderate average power of 100 mW, it is possible to achieve a pulse energy of 12.5 nJ and an ultrahigh peak power of 12.5 kW.

In addition, compared to lamp illumination in bright field microscopes, the use of modern femtosecond lasers as a light source in nonlinear optical microscopes also introduces the spatial method of enhancing excitation intensity for nonlinear optical signal generation. Spatial coherence is one of the most important properties of a laser, which is demonstrated by the laser output being a unidirectional beam. Therefore, when applied as a light source in microscopy, lasers with good spatial coherence would be focused by an objective into a single diffraction-limited spot, which achieves a much higher local intensity inside the focal volume compared to the wide-field illumination by lamps. Suppose a laser beam with 1 W energy is focused to a diffraction-limited Airy disk with $1\,\mu m$ radius. Its intensity inside the Airy disk is approximately 3.18×10^{11} $W\cdot m^{-2}$, which is much higher than the condensed light intensity from a lamp (approximately 3×10^{5} $W\cdot m^{-2}$). However, to acquire a full-field image with this small laser focus point, either the laser direction or the specimen itself needs to be moved, which can be implemented

by scanning mirrors or translational stages, respectively. Plus, due to mechanical limitations, scanning mirrors can direct a laser focus to cover the same imaging field-of-view (FOV) much faster than moving a specimen by translational stages, and this microscope setup is named a laser scanning microscope. In this intraoperative imaging project, due to the limited acquisition time in the operating room, a high-speed laser scanning microscope design was chosen over a stage-scanning microscope.

In a wide-field microscopy setup, as illustrated in Figure 1.5 (A), multi-directional beams generated from an illumination lamp are focused onto the entire FOV through lenses and an objective. Reflected beams carrying optical information of the specimen are collimated and form an image of the specimen on the detection camera that records the captured image data. In this microscopy setup, the entire imaging FOV is illuminated at the same time by the multi-directional illumination lamp, without any scanning process. Therefore, the imaging speed of this microscope is high, and only limited by the acquisition rate of the camera. However, the disadvantages are obvious for this setup too. The lamp, as an inefficient light source, provides a uniform illumination field in a range of directions. Part of its power is blocked upon passing through the apertures of optics. The remaining power is distributed over the imaging field-of-view, which yields a rather low light intensity on the specimen.

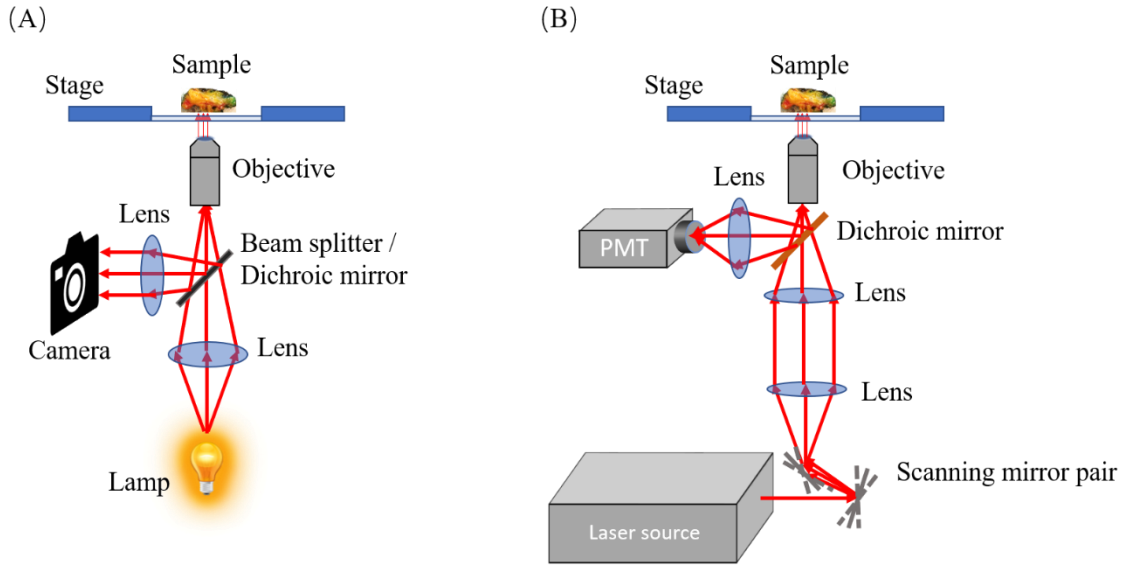

Figure 1.5 System schematics of (A) a wide-field microscope, and (B) laser-scanning microscope. PMT: photomultiplier tube. Scanning mirror pair contains two mirrors separately for two orthogonal scanning directions.

An ultrafast laser-scanning microscope, however, provides ultra-high optical intensity on the specimen by confining the photons in both space (transform-limited focal spot) and time (ultrashort pulse). In Figure 1.5 (B), the beam containing the femtosecond laser pulses is scanned by galvanometer-driven scanning mirrors (GALVO) and relayed onto the specimen by lenses and an objective. In the imaging focal plane, the laser beam is focused to a diffraction-limited spot and scanned to cover the entire imaging FOV. Imaging signals are reflected by a dichroic mirror (DM) and focused onto the detection window of a photomultiplier tube (PMT). Under this setup, images are mosaiced pixel-by-pixel via synchronized laser scanning and time-gated PMT recordings. Therefore, imaging speed is primarily limited by the speed of the laser scanning. For label-free nonlinear optical imaging modalities like 3PF and THG that utilize higher-ordered nonlinearities, another limitation is the relatively low generation rate of the nonlinear photons.

2 Intraoperative multimodal nonlinear optical imaging system

In this chapter, the detailed design and construction process of the intraoperative multimodal nonlinear optical imaging system is presented. This system is designed to overcome the limitations of using a lab-based multimodal nonlinear optical imaging system to capture the structural and molecular changes in fresh tissue, which begin to change and degrade immediately after removal from the body. Considerations like compact size, mobility, fast deployment, and light concealment are taken into account before and during system building. When finished, and before using it in a clinical setting to collect intraoperative imaging data, this system was tested in the lab to characterize its capabilities and parameters such as imaging FOV, axial and lateral resolution, and imaging acquisition speed. Laser safety standards are also strictly met to prevent any laser-induced operator injury or damage of the tissue being imaged.

2.1 Motivations

There are two major motivations to build this intraoperative imaging system. First, the imaging modalities SHG, THG, 2PF, and 3PF have already been successfully integrated into a single-source microscopy imaging system that found great potential in stain-free histopathology [4] and imaging the tumor microenvironments [5]. However, as was mentioned in the previous chapter, the tumor microenvironment study focusing on EVs was mostly demonstrated on a rat mammary tumor model. Imaging studies involving human subjects and human tissue specimens offer more clinical significance, but are often limited due to the artifacts induced during tissue preservation after surgical excision.

Second, several applications using nonlinear optical imaging in intraoperative settings have been demonstrated in recent studies to achieve clinical goals like tumor margin assessment [7, 8] and tumor type diagnosis [7]. Label-based nonlinear optical imaging and stimulated Raman scattering (SRS) imaging have been utilized in these applications to achieve rapid and high-contrast imaging. However, low-contrast and optically insensitive structures in the tumor microenvironments like EVs have been largely neglected. In label-based nonlinear optical imaging, the signals generated from the labeling agents

completely overwhelm the EV signal, while SRS imaging fails to provide enough contrast for nanometer-sized EVs due to its low sensitivity. Therefore, this area of intraoperative label-free nonlinear optical imaging of the human breast tumor microenvironments is still awaiting investigation.

2.2 System design

2.2.1 Compact and robust modification of a multimodal nonlinear optical microscope

The first and foremost design consideration is the compact size of the portable cart that would house the entire system. Considering that the bulky lab-based system setup occupies half of a 4'×10' optical table, certain compromises were needed for compact-size integration.

To achieve an optimal excitation spectral range, the lab-based simultaneous label-free autofluorescence-multiharmonic (SLAM) microscope [6], as shown in Figure 2.1, utilized photonic crystal fiber (PCF) to expand the laser spectrum to a supercontinuum and pass the supercontinuum pulses through a pulse shaper to select certain spectral ranges and compress the pulses to the transform-limit. This spectral manipulation process managed to generate a transform-limited femtosecond laser pulse covering 1080 to 1140 nm for optimal excitation efficiency of four nonlinear imaging modalities. However, the PCF and pulse shaper require a great deal of physical space to operate and are vulnerable to optical misalignment, which makes them the main obstacles for integration into a compact and robust cart.

Set-up/parameters	PMT 1	PMT 2	PMT 3	PMT 4
Filter (nm)	365-375	420-480	540-570	580-640
Dichroic mirror edge (nm)	409	506	570	750
Modality	THG	3PF	SHG	2PF
Targeted substances	Optical heterogeneity	NADH	Collagen	FAD

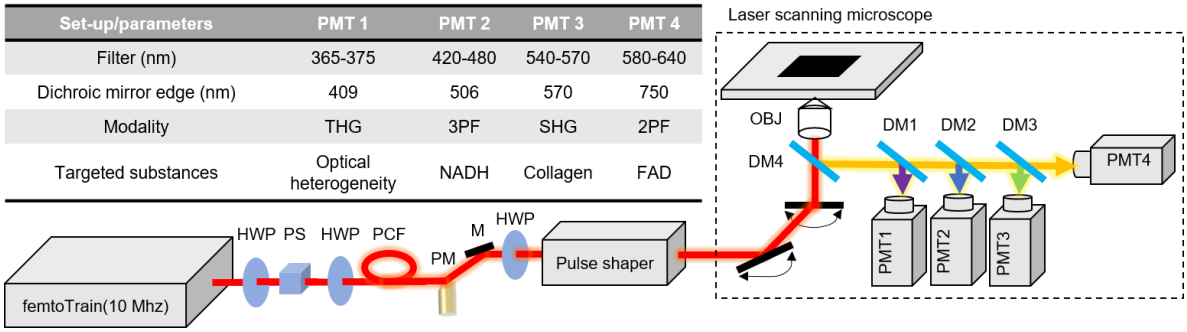

Figure 2.1 Schematic of the SLAM microscopy platform. The high-peak-power laser pulses were sent into the PCF to generate a supercontinuum. The pulse shaper is programmed to choose the excitation window (1080-1140 nm) and compensate the dispersion to make the output beam near-transform-limited. Different dichroic mirrors and optical filters are used in the detection system to collect spectrally resolved multimodal multiphoton signals by photomultipliers as specified in the table. DM, dichroic mirror; HWP, half wave plate; M, mirror; OBJ, objective; PCF, photonic crystal fiber; PM, parabolic mirror; PS: polarizer splitter [6].

The solution proposed is to use an alternative laser source that can generate transform-limited femtosecond laser pulses close to the optimal spectral range. A commercial fiber-laser (Fidelity-2, Coherent Inc.) was chosen as the laser source, which has a 1070 nm central wavelength, 70 nm spectral bandwidth, and 55 fs pulse duration at a pulse repetition rate of 70 ± 10 MHz [24]. In addition, this source has a built-in chirp-adjusting knob to keep the pulses transform-limited, and its maximum output power of $2\ \mathrm{W}$ is more than sufficient for intraoperative applications with fresh tissue. Finally, this laser has a cubical shape and is very compact compared to most commercial femtosecond lasers. Therefore, it is easy to fit it with other optical appliances on a 24"×24" optical breadboard inside the cart. Because the bulky and delicate PCF – pulse shaper combination, along with the four PMTs in Figure 2.1 designed for simultaneous detection of all four imaging modalities, takes more space than the cart can provide, a slower sequential detection of optical signals by a single PMT was implemented as a compromise to conform with the limited cart space.

To sum up, compromises were made to realize a compact and robust multimodal nonlinear optical imaging system, including the use of a more limited excitation spectral range by a single laser source, and a slower imaging acquisition speed by using only a single PMT. On the other hand, these compromises enabled for the first time an intraoperative label-free nonlinear imaging system that was compact and easy to operate, even in clinical settings such as the operating room.

2.2.2 Light concealment

The lab-based SLAM microscope is operated only in a completely dark environment, as PMTs are sensitive to any background light. Image signal-to-noise-ratio (SNR) would significantly decrease when acquiring images with the room lights on. However, it is infeasible to alter the illumination conditions in the operating room, which may affect the surgery. Therefore, it was necessary to build a light-tight portable imaging cart to block any background light, as well as prevent the laser beam from passing out of the cart, which may endanger the surgical staff and patients.

There are several aspects that need to be considered for light concealment. First, every part of the nonlinear optical microscope should be put inside the cart, including the objective, to make best use of the light concealment by the cart. Considering this, it is easy to choose between two major microscope setups: an upright microscope and an inverted microscope. Figure 2.2 shows diagrams of an inverted and upright microscope. In an upright microscope, specimens are placed underneath the objective and other optical hardware. Since tissue specimens are supposed to be accessed easily, it is more appropriate to be left outside of the cart, which makes everything above the specimen, including the objective, hard to be entirely blocked. With the inverted microscope configuration detecting a reflection or nonlinear signal, everything is placed under the imaging glass window, making it is easy to fit the entire optical setup in the cart, and then the sample is simply placed on the top surface of the cart. The imaging window was made of a thin cover glass and was used to hold tissues and transmit the laser beam. Because this cover glass is the only outlet for the light, background light and the exiting laser beam can be easily blocked by a small opaque plastic box. Another merit of using an inverted microscope in this application is that

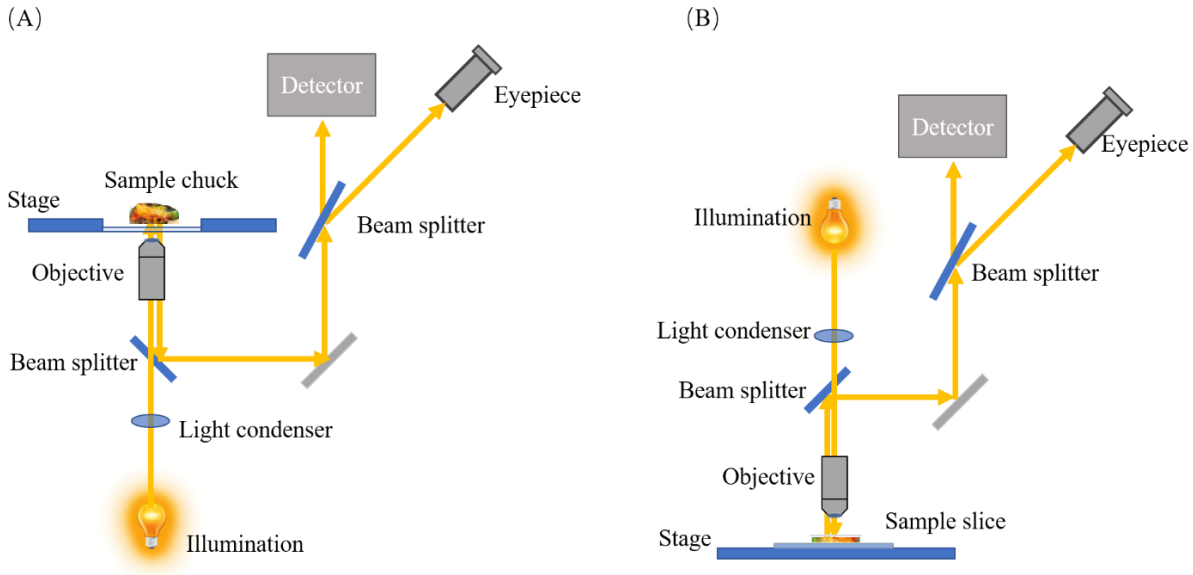

Figure 2.2 Diagrams of system schematics of (A) an inverted microscope, and (B) an upright microscope.

because of gravity, the weight of the tissue will automatically flatten the tissue surface that is in contact with the microscope cover glass, which creates a perfect plane for imaging.

Furthermore, in addition to the optical components, there are other critical components in the cart such as the computer, laser control, and galvanometer driver. The computer monitor was naturally located outside the cart for display and communication purposes. Connections between all of these components and the computer should be either wireless or deliberately concealed.

2.2.3 Motorized control

There are two critical adjustments needed before or during the acquisition of imaging data in the operating room: focus adjustment and imaging modality switch. In the intraoperative imaging system, any manual adjustment would break the light concealment, affect laser safety, and extend system operating time. Therefore, all these adjustments were implemented by motorized control.

Focus adjustment is a necessary process in all microscopy systems. As for a laser scanning microscope, real-time image acquisition serves as a critical feedback for focus adjustment. Manual focus adjustments would unavoidably necessitate openings in the cart enclosure, which could permit a large amount of background light into the cart. Therefore, a piezoelectric linear stage (SLC-24120, SmarAct GmbH) was used to implement vertical movement of the objective to adjust the focus plane. The stage enabled a fine focus adjustment with a step width of 1 – 1500 nm that is comparable to the system axial resolution, which was sufficient for acquiring sections that could then be assembled into stacks of images in 3-D.

As was mentioned in Section 2.2.1, the single-PMT setup required a sequential detection of the four imaging modalities that were differentiated by different detection wavelengths. Selection of the different detection channels was performed by switching the filter placed before the PMT. Motorized control of the modality switch was realized by a motorized filter wheel (FW102C, Thorlabs, Inc.). There were a total of six slots inside this filter wheel, enabling six different functions. First, four optical filters for the different imaging modalities were inserted into the filter wheel. Second, a solid metal piece

occupying the fifth slot acted as a shutter for the PMT. Finally, there was another imaging modality that was incorporated into the imaging system by using the empty slot. Without passing through any filter, light signals at all wavelengths reflected from the DM were sent to the PMT for detection. Because all nonlinear optical imaging signals are relatively weak, when no filter was used, the detected signal was the small portion of the original laser light reflected from the tissue. Therefore, this empty filter slot facilitated the detection of the conventional reflection or backscattered signal. Switch time between modalities was significantly shortened from around 20 seconds to one second with the implementation of this motorized control. In addition, this system, which utilized a femtosecond laser, was much safer without the frequent opening of the cart doors.

2.3 System setup

In this section, the system schematic is presented and thoroughly discussed to demonstrate the implementation of a rapid, reliable, and faithful nonlinear optical image system for use in intraoperative settings. Technical parameters of key components that essentially determine the major imaging characteristics are illustrated in separate sections. Figure 2.3 includes a general description of the imaging system.

(A)

(B)

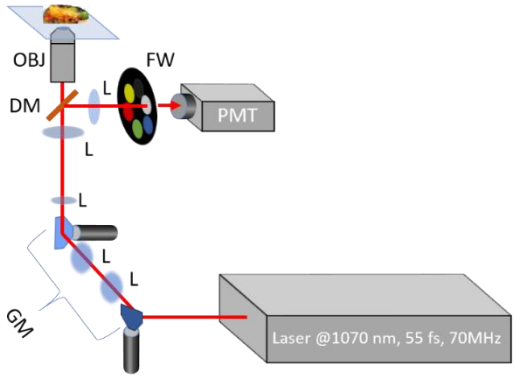

(C)

Modality	THG	3PF	SHG	2PF
Filter wavelength / nm	330 - 380	420 – 470	510 – 560	590 – 740

Figure 2.3 Design of the intraoperative label-free multimodal imaging system. (A) Photograph of the portable label-free multimodal nonlinear imaging system. (B) System schematic. (C) Transmission wavelengths of the four nonlinear optical imaging modalities. L: lens; GM: galvanometer-driven mirror; DM: dichroic mirror; OBJ: objective; FW: filter wheel; PMT: Photomultiplier tube.

2.3.1 Laser source

The laser source used in this intraoperative imaging system was a commercial fiber-laser (Fidelity – 2, Coherent, Inc). This source provided transform-limited 55 femtosecond (fs) laser pulses with a spectral range of 1040 - 1100 nm [24]. This near-infrared (NIR) wavelength band lies in the second optical window that is found to have low absorption and scattering coefficients in biological tissues [25]. Therefore, by using this laser source, nonlinear optical interactions were excited and detected to a greater depth in biological tissues compared to using a laser with wavelengths out of any tissue optical window, which subsequently increased the maximal depth of image acquisition. In addition, while the structural information visualized by the two multi-harmonic generation processes (SHG and THG) was independent of the excitation wavelengths, a specific spectral range is required to excite the autofluorescent biomolecules. Through two-photon or three-photon absorption processes, this commercial laser was able to provide effective excitation to major endogenous fluorophores in biological tissues like FAD, NADH, ceroid (lipids), and elastin. The one-photon excitation and emission maxima of these endogenous fluorophores are included in Table 2.1. First, NADH and ceroid, as indicated by their one-photon excitation maxima, can be excited by the three-photon absorption from this laser. FAD, however, has a maximum excitation wavelength outside of the two-photon absorption spectrum provided by the laser from 520 nm to 550 nm. Nonetheless, the 2PF signal generated from FAD was still strong enough to be effectively detected. As for elastin, although its single-photon excitation wavelengths coincided with the three-photon excitation wavelengths provided by this laser, its fluorescent signal generated through three-photon excitation was found to be much weaker than that through two-photon excitation. The reason for this mismatch is that the single-photon excitation spectrum of elastin extends to the longer wavelengths that are related to the two-photon excitation of the laser [26], which has a lower excitation efficiency than the two major local excitation maxima wavelengths 290 and 325 nm. Even with this lower excitation efficiency, because of the large difference in excitation cross sections resulting from the different orders of optical nonlinearities, the fluorescent signal from elastin was mostly generated through two-photon excitation with longer wavelengths than through the values shown in Table 2.1. Other reasons for this

may include higher effective absorption cross section and quantum efficiency of elastin for 2PF. Other endogenous fluorophores like tryptophan and tyrosine, also included in Table 2.1, can be excited by even shorter wavelengths, and likely correspond to four-photon excitation processes, which are extremely weak and essentially undetectable.

In addition, the short duration and transform-limited shape of the laser pulses offered a high peak power up to 4.5 kW for a higher excitation efficiency, while keeping a relatively low average power of 10 mW, under the laser safety standard limit found by the America National Standard Institute (ANSI) [27]. To sum up, spectral and temporal characteristics of the laser source contributed to a greater imaging depth in biological tissues and an effective multiphoton excitation for tissue structures and major fluorescent biomolecules.

The spatial parameters of the emission laser beam were also taken into account for better imaging performance. First, the beam emitted from this laser was linearly polarized in the horizontal direction [24]. Therefore, a half wave plate (AHWP05M-980, Thorlabs, Inc.) was used to arbitrarily alter the direction of linear polarization for attenuation purposes. A polarizing beam splitter (CCM1-PBS253, Thorlabs, Inc.) was placed after the half wave plate to transmit the horizontally polarized beam while reflecting the vertically polarized beam to a beam block (LB1, Thorlabs, Inc.). This setup was used to attenuate the high-power output laser beam without causing any heating or damaging effect. With this setup, a horizontally polarized laser beam was sent to the specimen, and no polarization-sensitive detection was included in this imaging system. Second, the laser beam diameter under the $1/e^2$ standard was 1.2 ± 0.2 mm [24], which was small enough to be entirely reflected by the galvanometer-scanning mirrors. However, smaller beams were not always preferred because of the beam expansion setup introduced in Section 2.3.2. Finally, this laser beam had a high-quality Gaussian beam profile with the beam quality factor M^2 less than 1.2, a beam circularity from 0.9 to 1.1, and an astigmatism less than 10% [24]. These technical parameters indicated that the laser beam of this source had very little deviation from a perfect Gaussian beam, which essentially would not affect imaging quality.

In conclusion, this compact and robust fiber-laser satisfied the basic requirements of the multimodal nonlinear optical imaging as well as the ANSI standard for laser safety. Image data could be acquired from a greater depth because the laser wavelengths were within the optical window of biological tissues. Moreover, the linearly polarized beam facilitated a safe attenuation method of the output power. The spatial profile of this laser beam enabled non-truncating beam scanning and restrained the imaging aberrations normally caused by beam variation from an ideal Gaussian beam.

Table 2.1 Excitation and emission maxima of common autofluorescent molecules

Molecule	Single-photon excitation (nm)	Two-photon excitation (nm)	Three-photon excitation (nm)	Emission (nm)
NADH	290, 351 [28]	730 [2]	1040 [22]	440, 460 [28]
FAD	450 [28]	900 [2]	-	535 [28]
Elastin	290, 325 [28]	740-750 [21], 860 [15]	-	340, 400 [28]
Tyrosine	275 [28]	-	-	300 [28]
Tryptophan	280 [28]	580 [29]	750 [21]	350 [28]
Ceroid	340-395 [28]	-	<700 [21]	430-460, 540 [28]

"-" represents that there is no well-measured value to fill in this blank.

2.3.2 Beam scanning and relaying system

After the generation and emission of the laser pulses, the beam of pulses needed to be scanned and relayed before reaching the back aperture of the imaging objective. A pair of galvanometer-scanning mirrors (62xxH Series Galvanometer XY Sets, Cambridge Technology, Inc.) and four lenses (Achromatic doublet, C-coated, Thorlabs, Inc.) were used to achieve this goal. A galvanometer-scanning mirror is a type that changes its orientation according to different applied voltages or waveforms, and its maximal scanning speed is normally limited by the mechanical inertia and stability. The attenuated laser beam reached the center of the first galvanometer-scanning mirror and is scanned along the X axis (X GALVO). A pair of identical lenses with focal lengths $f = 50\ \text{mm}$ (AC254-050-C, Thorlabs, Inc.) were inserted between the two galvanometer-scanned mirrors, with a distance of $2f$ between them. The two galvanometer-scanning mirrors were respectively placed at the back focal plane of this lens pair, forming a $4f$ system. The function of this $4f$ system was to relay the scanning beam spot along the X axis from

the X galvanometer-scanning mirrors to the second mirror scanning along the Y axis (Y GALVO). In other words, this $4f$ system formed an image of the X GALVO onto the Y GALVO. Therefore, with the scanning of the two GALVOs, the laser beam afterward could be viewed as the beam emitted from a laser source placed at the fixed plane on the Y GALVO with the emission direction scanning along the two dimensions: X axis and Y axis. Then, this 2D scanning laser beam passed another $4f$ system, which had two lenses with different focal lengths. In this case, lenses with focal lengths of 30 mm (AC254-030-C, Thorlabs, Inc.) and 150 mm (AC254-150-C, Thorlabs, Inc.) were chosen to expand the original beam diameter of 1.2 ± 0.2 mm that was measured under the definition of the $1/e^2$ width [24]. At the back focal plane, the laser beam diameter was expanded by a factor of five to reach the diameter of the back aperture of the objective (approximately 8 mm) and therefore fully utilize the numerical aperture that is available by the objective. In addition, the fixed virtual 2D-scanning laser point source on the Y GALVO was projected onto the back focal plane of the second $4f$ system where the objective was placed. Each individual direction of the laser beam within the 2D-scanning range corresponded to a specific focal point on the sample inside the FOV. Notably, all four lenses used here were achromatic doublet lenses with a NIR coating (Achromatic doublet, C-coated, Thorlabs, Inc.) designed for a transmission spectral range of 1050 – 1620 nm, which covered the laser wavelength. In general, if the laser beam was fixed, it could be aligned to pass through the center of any lens, and most often, the simplest singlet lenses could meet all requirements. However, since this laser beam was scanned for imaging, and a wide scanning angle was always preferred for a large FOV, the achromatic doublet lenses were used to correct chromatic and spatial aberrations caused by the wide spectral range and large scanning angles, which essentially enlarged the imaging FOV and enhanced the image quality. With the scanning and relaying optics, the laser beam fully filled the back aperture of the imaging objective, and generated a 2D focal point scanning pattern in samples to provide excitation within the entire imaging FOV.

2.3.3 Objective

As a key optical component in all microscopes, the objective used in this imaging setup was selected to be the XLUMPLFLN 20X from Olympus, Inc. This objective is a water-immersion objective with a 20× magnification, a numerical aperture (NA) of 1.0, and good transmission at NIR wavelengths. There were several reasons to use this specific objective in the intraoperative system. First, the relatively low magnification ratio yielded a larger FOV under the same scanning angle of the GALVO mirrors. In this intraoperative imaging project, a larger imaging FOV was preferred over higher magnification to cover larger areas on a specimen within the limited acquisition time. Second, the 1.0 NA of this objective was sufficient to achieve a lateral and axial resolution at the micrometer-level. Detailed calculations and tests of resolutions are present in Section 2.4. Finally, the transmission through this objective was good for both the original excitation wavelength around 1070 nm and the wavelengths of the nonlinear optical signals. As plotted in Figure 2.4 [30], except for the THG signal (330 – 380 nm), the wavelengths of the other imaging modalities as well as the excitation source can pass through this objective with a

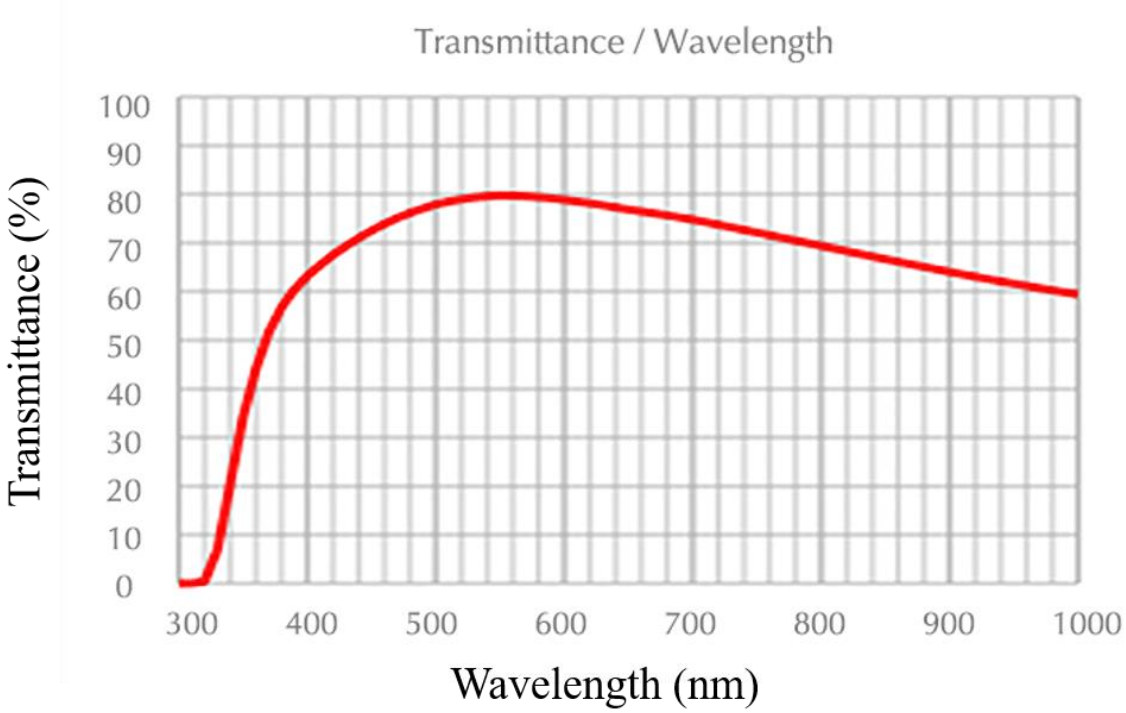

Figure 2.4 Optical transmittance of the Olympus XLUMPLFLN 20X objective used in the nonlinear microscope, with the horizontal axis representing wavelength in nanometers. Modified from [30].

transmittance higher than 60%. There were other commercial objectives specifically designed for broadband transmission, but very few of them were cost-effective and had other favorable parameters like this one. The objective was placed on a linear piezo stage (SLC-24120, SmarAct GmbH) moving along the vertical direction for automatic focus adjustment. However, because the focus adjustment was realized by altering the distance from the objective to the specimen, the objective experienced a certain deviation from the back focal plane of the beam relay system. The beam truncation induced by the objective deviation caused a smaller FOV and lower sensitivity. The ideal method of focus adjustment was to vertically move the specimen instead of the objective by a translational microscope stage, which would maintain the optimal location of the objective. Fortunately, because the maximal imaging depths of all imaging modalities were less than 1 mm, the beam truncation induced by this small objective displacement did not cause any noticeable reduction of the image FOV.

2.3.4 Detector

The nonlinear photons were produced in a specimen, and some of them were either generated in the backward (epi-) direction or back-scattered to enter the objective lens placed underneath the specimen. After passing through the objective lens, these nonlinear photons along with some original laser photons reached the front surface of the dichroic mirror (DCM) that reflected these nonlinear photons with wavelengths under 800 nm and transmitted the original laser photons at a wavelength around 1070 nm. Before reaching the detection window of the PMT, further spectral selection was implemented by the optical filters inside the filter wheel. Transmission bands of the four optical filters for the different imaging modalities are shown in Figure 2.3 (C). The spectral ranges of the optical filters for the two fluorescence imaging modalities (2PF and 3PF) were deliberately determined to effectively detect the fluorescent signals from the autofluorescent biomolecules (Table 2.1) with minimal spectral overlap, while the filtered spectral ranges of the two multi-harmonic generation imaging modalities were simply calculated by dividing the excitation wavelength band (1040 – 1100 nm) by the number of two or three for SHG or THG, respectively. Comparing the spectra of autofluorescent molecules in Table 2.1 with the

transmission bands listed for each optical filter in Figure 2.3 (C), it is found that the fluorescence emission of FAD and NADH, albeit the partially overlapping spectra, were separately detected by the 2PF and 3PF filters without any spectral overlap. In addition, as discussed in Section 2.3.1, because the fluorescence from elastin was excited by longer wavelengths compared to the value in Table 2.1, the fluorescence was also detected in the 2PF imaging modality with longer wavelengths than the emission maxima included in Table 2.1. Finally, ceroid, as a specific kind of lipids, was primarily detected in the 3PF imaging modality.

Filtered nonlinear optical signal corresponding to each imaging modality was detected by the PMT (H7421-40, Hamamatsu Photonics). The PMT utilized the photoelectric effect to convert the incident photons into electrons, and then amplified the electron fluence by dynodes sequence via secondary emission. As a result, each signal photon appeared as a short pulse of electric current or voltage signal at the PMT output. For a higher detection sensitivity of the nonlinear photons, the more sensitive photon-counting PMT was preferred over the faster but less sensitive analog PMT.

2.3.5 Software control

In addition to the hardware selection and optical alignment discussed above, software control of the image data acquisition was another essential task in this intraoperative imaging project. A lab-developed LABVIEW VI was used to realize the rapid and reliable image acquisition and enable the adjustment of various imaging parameters.

Optical and mechanical components that communicated with the computer included the GALVOs, PMT, objective stage, and filter wheel. In particular, the first two were the key components in this image acquisition VI, while the last two were independently controlled by other programs or software. The data acquisition (DAQ) cards (PXI-6239, National Instruments Corporation) were used to communicate with these components. Unlike the built-in USB and RS232 ports of a computer, the DAQ cards, connected to the computer through the PCI Express slots, are specialized for high-speed and large-volume data acquisition. The commonly used functions of DAQ cards include using a built-in external

clock to generate highly synchronized signal sequences by proper triggering and counting the number of voltage or current signal pulses within a certain amount of time. In the image acquisition VI, the two galvanometer-scanning mirrors received analog voltage signals from the two analog outputs of a DAQ card, with the X GLAVO acting as the pixel scanner and the Y GALVO as the line scanner. In addition to the waveform, synchronization of these signals was equally critical to image acquisition. To implement perfect synchronization, both analog signals received triggers from two synchronized square wave sequences generated by four counters built into the DAQ cards.

In Figure 2.5, the line scanning analog signal shown in the third row changed values upon being triggered by the rising edges (red dashed lines) of the square wave sequence with the name of "line gating signal". Likewise, the pixel scanning signal for the pixel scanner increased with the rising edges (black dashed lines) of the other square wave sequence shown as the pixel gating signal in Figure 2.5, and was set to its initial value when the falling edges (green dashed lines) of the line gating signal were detected. In this setup, synchronization of these two gating signals was implemented by using the rising edges (red dashed lines) of the line gating signal as the starting triggers for the pixel gating signal and the falling

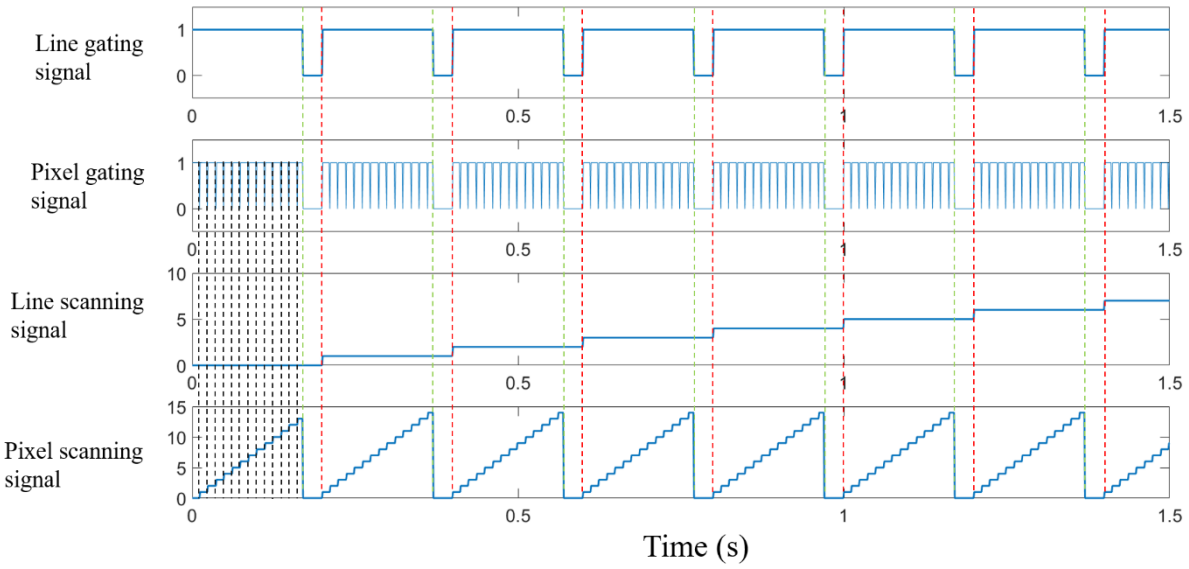

Figure 2.5 Waveforms and synchronization of the square gating signals and analog scanning signals. Red and green dashed lines mark the starting and ending time of each scanning line, and black dashed lines mark the starting edge of each pixel gate in the first line.

edges (green dashed lines) as the ending triggers (Figure 2.5). With the synchronization of the two gating signals, the two analog scanning signals were also synchronized through the triggering setup. Therefore, the two galvanometer-scanning mirrors driven by these analog scanning signals were accurately scanned to generate a 2D scanning pattern at the objective focal plane.

Apart from triggering the line and the pixel scanning signals, these two square wave sequences were also used to provide gates for photon counts detected by the PMT. The PMT sent voltage signal pulses to a counter on the DAQ card that continuously counted the number of pulses at a high speed. Initialized by a rising edge of the pixel gating signal, the counter recorded the current value of the photon count at the time of this rising edge, and reported a new value at the following falling edge. Differences between these two values of photon counts represented the signal intensity of this individual pixel, which was sent to the computer to be registered in the image matrix. After acquisition of each single image, all signals were initialized and re-started for the next image acquisition cycle.

The technical parameters like pixel size, scanning frequency, and number of pixels per line, were made adjustable in this image acquisition VI. As a result, the imaging characteristics like FOV, digital resolution (different from the optical resolution defined by the diffraction limit) and acquisition speed could be arbitrarily manipulated for different purposes. For example, when adjusting the imaging focus, one needed to constantly observe the change of the acquired images caused by the moving focal plane. In this case, a large pixel size, a small number of pixels per line, and a high scanning frequency were used to display low-quality images of the specimen at a high speed. However, for intraoperative image data acquisition, pixel size was set sufficiently small to fully utilize the optical resolution of the imaging system, a sufficient number of pixels per line was selected to cover the maximal FOV determined by lens aperture, and the scanning frequency was determined to achieve a high signal intensity and a moderate image acquisition speed.

2.4 Imaging performance test

In this section, the basic imaging characteristics such as lateral and axial resolution, FOV, and image acquisition speed were tested, derived, and compared with theoretical values to evaluate performance of the imaging system and to provide evidence for characterization of intraoperative image data.

2.4.1 Lateral resolution

Because of the nonlinear dependence on optical intensity, nonlinear optical imaging generally has a smaller lateral point spread function (PSF) than in conventional microscopy, and therefore offers a higher lateral resolution. Moreover, powers of intensity dependence vary with different nonlinear imaging modalities. In this imaging system, imaging modalities with a higher order of optical nonlinearity, like THG and 3PF, tend to have a higher lateral resolution than those with a lower one. The lateral resolution of each nonlinear optical imaging modality was calculated based on the experimental results from the conventional reflection imaging modality.

A standard 1951 United States Air Force (USAF) resolution target was used to test lateral resolution of intraoperative imaging system. Comparing with the standard printed image of Groups 6 to 9 from the USAF resolution target (Figure 2.6 (A)), the reflection microscope image in Figure 2.6 (B) managed to display most of the line pairs and features. In particular, the line pairs in Groups 8 and 9 were marked by the red dashed box in Figure 2.6 (B). To test the lateral resolution of this intraoperative imaging system, it was necessary to examine the visualization result of the resolvable line pairs with the smallest width. Therefore, an image visualizing the high-resolution Groups 8 and 9 was acquired at a lower scanning speed (Figure 2.6 (C)), with the yellow dashed box encircling the three line pairs that were likely to be the smallest resolvable line pair. In comparison with Figure 2.6 (A), these line pairs in the yellow dashed box were obviously corresponding to Elements 4 to 6 of Group 8. By examining the enlarged image (Figure 2.6 (D)) and the processed binary image (Figure 2.6 (E)) of the line pairs in

Elements 4 to 6 of Group 8, the smallest resolvable line pair was determined to be in Element 5 of Group 8. The averaged line plot for one of the line pairs (within the blue dashed box in Figure 2.6 (D)) in Element 5 of Group 8 is shown in Figure 2.6 (F), containing three local peaks that represent the bright lines in this line pair. According to the information on the USAF resolution standard, the width of the lines in Element 5 of Group 8 is about 1.23 μm. The effective visualization of the line pair of 1.23 μm single-line width serves to characterize the full width at half maximum (FWHM) resolution of this conventional reflection imaging modality to be approximately 0.615 μm. The theoretical lateral resolution of conventional reflection microscopy under the FWHM definition can be approximately calculated by

$$FWHM_{conventional} = 0.51\frac{\lambda}{NA} \approx 0.55\,\mu\text{m}, \tag{2.1}$$

which is close to the lateral resolution that was characterized using the USAF resolution target.

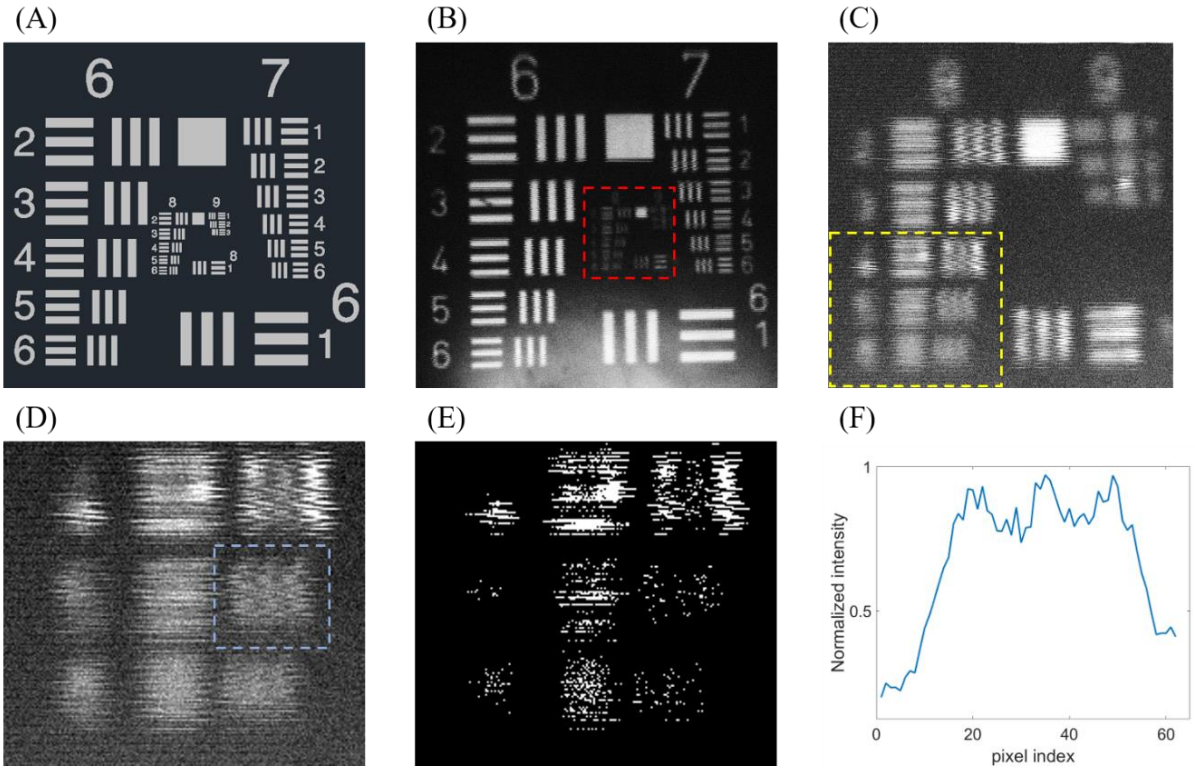

Figure 2.6 Characterization of resolution using the USAF resolution target. (A) Standard printed image of USAF resolution target (Groups 6 to 9). (B) Reflection microscopy image of USAF resolution target (Groups 6 to 9). The red dashed box encircles the Groups 8 and 9. (C) Enlarged image of Groups 8 and 9. The yellow dashed box encircles the line pairs in Elements 4 to 6 of Group 8. (D) Enlarged image of line pairs in Elements 4 to 6 of Group 8. The blue-dashed box marks the smallest resolvable line pair (Element 5 of Group 8). (E) Binary image of (D). (F) Averaged line plot of the line pair marked by the blue dashed box in (D). Three peaks were identified in this plot.

Utilizing the lateral resolution characterized by the conventional imaging modality, the lateral resolution of the four nonlinear optical imaging modalities was calculated or approximated accordingly. First, the $1/e$ lateral resolution of 2PF was calculated using the equation [31]:

$$\omega_{xy} = 0.325 \frac{\lambda}{\sqrt{2} NA^{0.91}}, \tag{2.2}$$

which yields a theoretical value of 0.49 μm or a value of 0.98 μm if one were to use the experimental lateral resolution of conventional reflectance imaging to estimate the resolution for 2PF. The conversion factor between FWHM and $1/e$ resolution is approximately 0.83, which was used to compare the resolution defined under these two resolution standards. Second, considering that 3PF in this setup was excited by the same illumination wavelength as 2PF, its $1/e$ lateral resolution for thick tissue was found to be 48% higher than that of 2PF [32], which would be 0.51 μm for the estimated value based on conventional reflectance imaging and 0.26 μm for the theoretical value. Third, SHG microscopy was found to have a 26% lateral resolution improvement in comparison with conventional microscopy [33], which helps derive the estimated and theoretical FWHM lateral resolution of SHG imaging in this system to be 0.81 μm and 0.41 μm, respectively. Finally, because of the similar mechanism behind SHG and THG, the lateral resolution of THG is approximated to be 0.6 μm for the estimated value and 0.3 μm for the theoretical value. Notably, the estimated lateral resolutions calculated for each imaging modality are only conservative approximations based on the USAF resolution target measurements. The real experimental limit of lateral resolutions could be further characterized by using nanometer-scale beads that emit nonlinear signals. However, the lateral resolutions measured were sufficient to assess the overall performance of this intraoperative imaging project.

2.4.2 Axial resolution

The axial resolution determines the optical sectioning ability of the nonlinear optical imaging modalities. In histology, the paraffin-embedded tissues are normally sectioned into 5 μm slices to get a clear single-cell-thickness view under the wide-field microscope. Therefore, to achieve at least the same

imaging quality at different focal depths, the axial resolutions of the nonlinear optical imaging modalities were required to be under 5 μm.

A group of fluorescent beads with 1 μm diameter was imaged using 2PF. The images were acquired at different depths of focus (Figure 2.7 (A)), which revealed the relationship between imaging depth and peak amplitude at the center area of the beads, as well as the depth-dependent bead diameter as it appeared in each image. Compared to the axial PSF of a conventional microscope, the amplitude of the axial PSF of a 2PF microscope has a power of two on the sinc function:

$$PSF_z(z) = \left|\mathrm{sinc}\left(\frac{2\sin^2(NA/2)}{\lambda_0} z\right)\right|^2 . \tag{2.3}$$

As is shown in Figure 2.7 (B), the depth-dependent peak amplitude data were average-filtered, normalized, and then fitted using a basic form of Eqn. (2.3):

$$y = \left|\mathrm{sinc}(a*(x-b))\right|^2 , \tag{2.4}$$

with a relating to the effective NA of 2PF imaging and b representing the relative axial position of the center of a fluorescence bead. Fitting curves of eight beads showed good fitting qualities with the R-squared values of 0.85 ± 0.072. Fitting curves yielded the average values of fitting parameters with standard deviations that were $a = 0.44 \pm 0.086$ and $b = 10 \pm 0.91$. Using the values of a, the effective NA of 2PF imaging in this system was calculated to be 1.0 ± 0.11, which was substituted into the equation for axial resolution:

$$FWHM_{axial} = \frac{1.3\lambda_0}{NA^2} \approx 1.4 \pm 0.32 \text{ μm.} \tag{2.5}$$

The theoretical axial resolution of 1.4 μm using the labeled NA of the objective is equal to the measured experimental axial resolution, which indicates a good optical alignment that fully utilizes the NA of the objective. The axial resolution of 3PF was calculated to be between 0.84 μm and 1.1 μm based on a study of 3PF imaging resolution improvement [32].

Furthermore, the axial beam profile of a focused Gaussian beam provided another means of

describing axial resolution. As is shown in Figure 2.7(C), beam diameter $2w$ was fitted versus depth z using the axial beam profile function of a Gaussian beam with a goodness of fit of 0.77 ± 0.10:

$$w = w_0\sqrt{1+\frac{(z-d)^2}{z_R^2}}, \tag{2.6}$$

which was used to calculate the diameter of the beam waist w_0, depth of beads d, and Rayleigh range z_R. The confocal parameter $2z_R$ is calculated to be 4.4 ± 1.7 μm. Because of the phase-matching

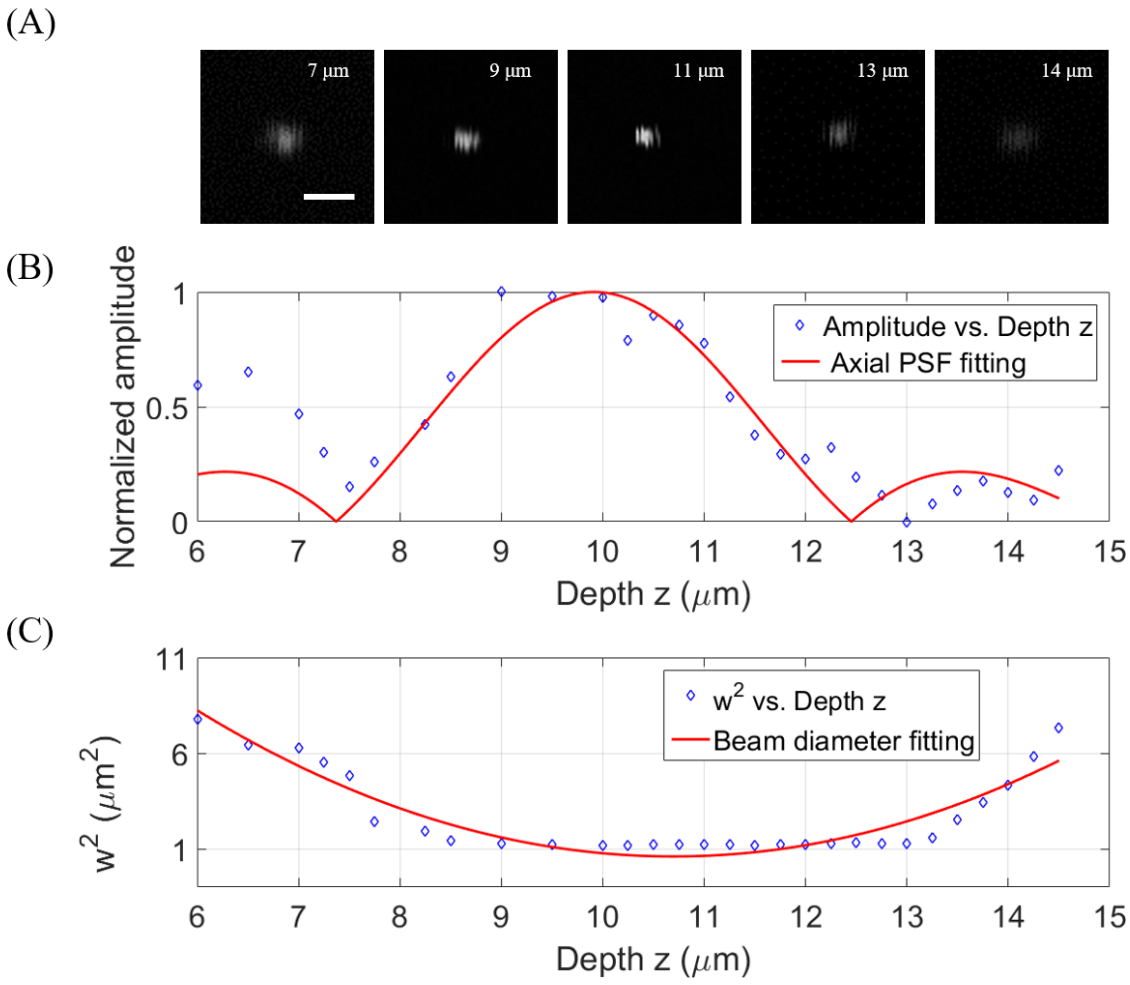

Figure 2.7 Characterization of axial resolution using fluorescent beads of 1 μm diameter. (A) 2PF-contrast images of fluorescent beads at various relative depths (white text at upper-right). (B) Normalized amplitude of beads changes with different depths and a fitted PSF curve (R^2=0.80). (C) Depth-dependent squared diameter w^2 of beads and the fitted Gaussian beam axial profile (R^2=0.69). Scale bar in (A): 5 μm.

condition, the axial resolutions of the two multi-harmonic generation imaging modalities were approximated according to their nonlinear dependence on the illumination intensity. For SHG, the diameter of the excitation volume can be approximately expressed as a quadrature version of Eqn. (2.6):

$$w_{SHG} = w_{SHG0}[1+\frac{(z-d)^2}{z_R^2}]. \tag{2.7}$$

The confocal parameter for this equation that yields $w_{SHG} = \sqrt{2}w_{SHG0}$ is $1.287z_R \approx 2.8\,\mu\text{m}$, which can be used to represent the axial resolution of SHG imaging. Similarly, the approximate axial resolution of THG was calculated to be $1.020z_R \approx 2.2\,\mu\text{m}$.

Notably, both fitting functions took into consideration the offset of depth read from the linear stage, which described the axial location of the bead centers. The value of the depth offset is represented by parameter b in the amplitude fitting and d in the beam diameter fitting. Through data analysis, the average value of b was found to be approximately 1 μm smaller than d. Therefore, the beads in the amplitude fitting results appeared shallower than in the beam diameter fitting. The most convincing reason for this is that the 2PF signal intensity generated from different depths underwent different amounts of attenuation before reaching the objective. The 2PF signals generated from the deeper regions were attenuated more than the signals generated from the shallower regions. Therefore, the overall positions of the beads appeared shallower in the amplitude fitting curves. Beam diameter, however, experienced less alteration during propagation, and thus would probably give a more faithful result of the axial positions of the bead centers.

2.4.3 Field-of-view

A grid target was imaged with up to the maximum scanning angle of the GALVO mirrors, and revealed the vignetting effects, which appeared at the four corners of Figure 2.8. In this image, there are approximately six squares along both the vertical and horizontal directions. Given that the grid bars are 100 μm apart, the maximum FOV of this intraoperative nonlinear optical imaging system was characterized to be 600×600 μm^2.

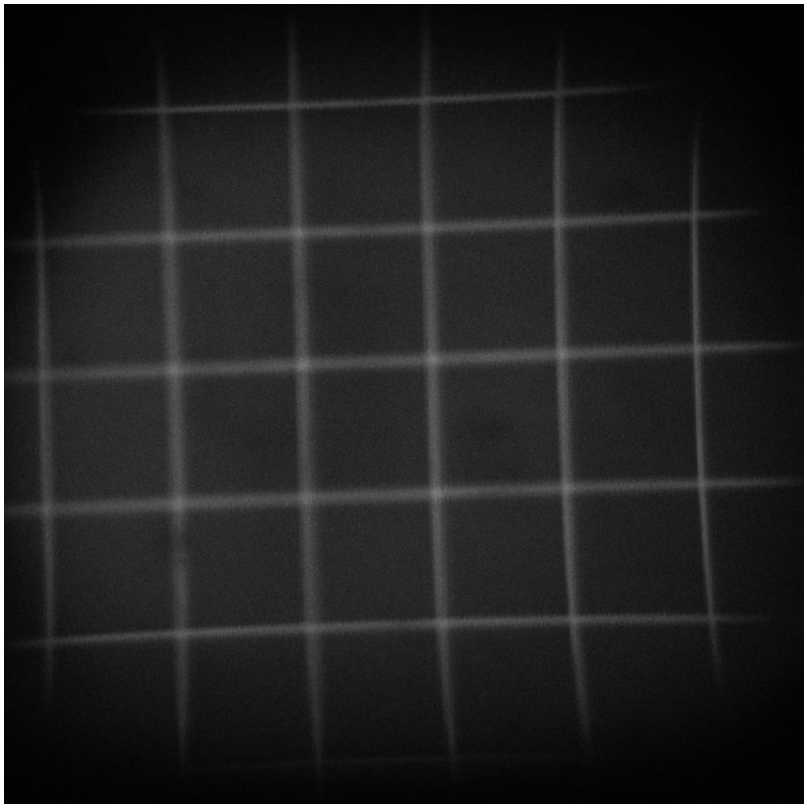

Figure 2.8 Image of a grid target with 100 μm grid spacing in both the vertical and horizontal directions.

2.4.4 Imaging acquisition speed

To keep the total imaging time within the restrictions in the operating room, imaging speed was maximized while maintaining high image quality. The same imaging speed was kept for all images acquired intraoperatively, which was around five minutes per imaging FOV, with each imaging modality taking approximately 80 seconds. Under this imaging speed, the updating frequency for the pixel scanning signal was about 25 kHz, the same as the frequency of the squared wave in the pixel gating signal.

In general, imaging speed in these systems may be limited by the temporal resolution of the detector, the maximum scanning frequency of the GALVO scanner, or the data transfer rate between the detector and the computer. However, none of these factors limited the image acquisition speed of this intraoperative system because the limiting factor was the low generation rate of the nonlinear photons, especially those from 3PF and THG. The average laser power of 10 mW under the ANSI laser safety

standard [27] restrained the maximum intensity of the nonlinear optical signals generated within a specimen. To acquire high-quality nonlinear optical images with moderate SNR, the dwell time for each pixel was substantially longer to receive more nonlinear photons. In addition, the pixel size was set to be 0.3 μm to take advantage of the optical lateral resolution, and the pixel number was chosen to be 2000×2000 to cover the full FOV (Section 2.4.3). To implement these parameters, galvanometer-scanning mirrors were programmed to scan at a low frequency over a large angular range with many periods of pixel gating signal in each line, and the counter on the DAQ card detected photon counts for each pixel at an extremely low rate compared to its full capacity (16-bit, 250 kilosample /second (kS/s)). The DAQ card used in this system has two analog output with a maximum update rate of 500 kS/s that is sufficient to generate the scanning signal for the pixel scanner (25 kS/s). In addition, the counters on this DAQ card could generate square waves with a frequency up to 20 MHz that is much higher than the required frequency 25 kHz of the pixel gating signal in this system. Finally, bit-depth of the counters (32 bit) supported the recording of photon counts sent from the PMT.

In conclusion, the image acquisition speed of this intraoperative imaging system was primarily limited by the photon generation rate of the nonlinear optical interactions and the required image SNR, sampling dimension, and FOV.

3 Label-free multi-contrast nonlinear optical images of human breast tissues

The intraoperative imaging system was used during breast cancer surgeries to acquire label-free multi-contrast images of human breast tissues. These intraoperative label-free images were compared to

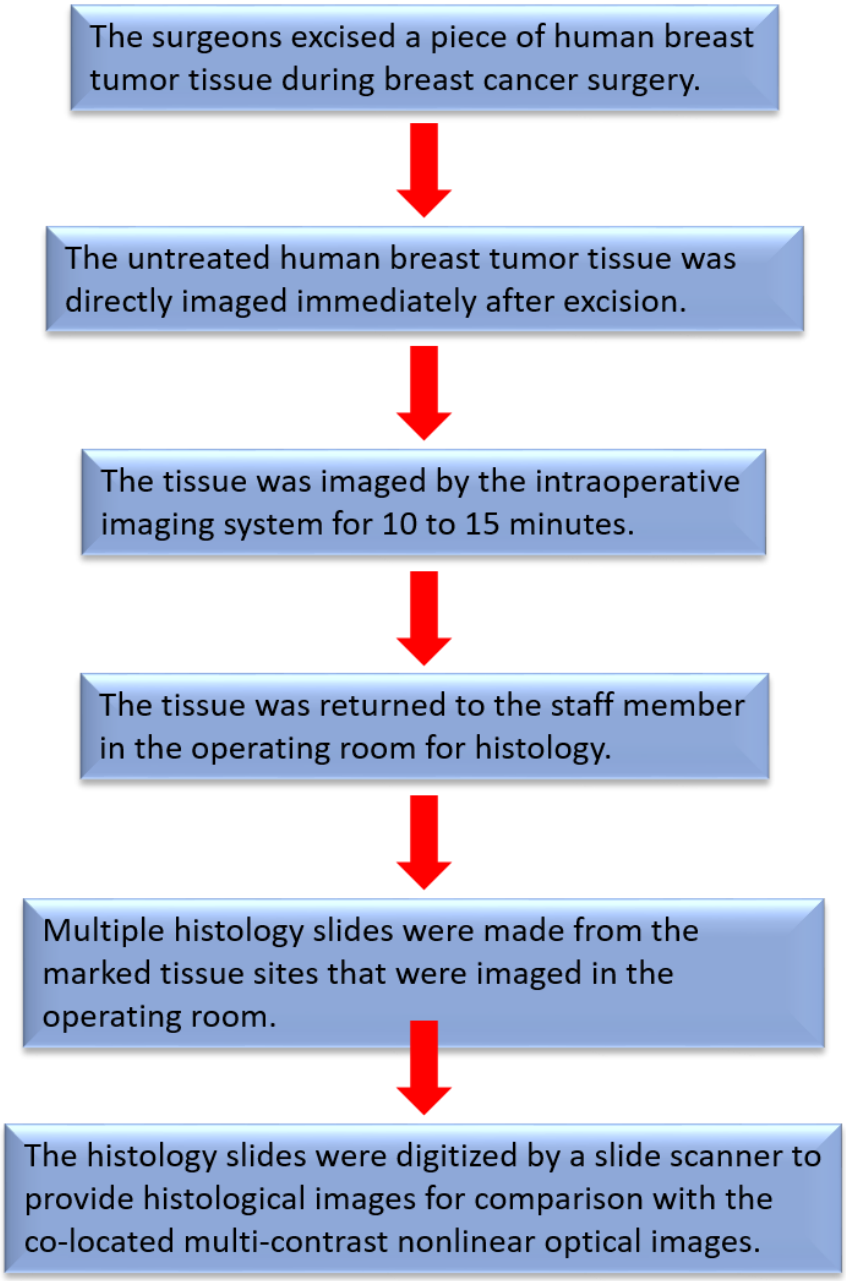

Figure 3.1 Flow chart of the intraoperative imaging, histology slide preparation, and characterization procedures.

the co-located histological images acquired two or three days later. Excellent correlations were identified between the two imaging techniques, which demonstrated the capability and credibility of the intraoperative imaging system. Intraoperative implementation of this imaging system did not perturb the surgical routine and workflow of these breast cancer cases because the nonlinear optical images were intraoperatively acquired within the time window of approximately one hour between the surgical excision and histology preparation. A complete set of procedures describing the intraoperative imaging and following histological tissue processing is presented in a flow chart (Figure 3.1).

Basic tissue features were characterized by their nonlinear optical signatures appearing in multi-contrast images. Combining different optical signatures from multiple imaging modalities, more complicated features of diagnostic interests such as the cytoplasm of tumor cells and tumor-associated collagen signatures (TACS) [34] were identified and correlated well with histology. Information on the tissue features characterized from the multi-contrast images was utilized to differentiate breast tumor subtypes by their subtle differences and to recognize both benign and malignant events occurring in tumor microenvironments.

The visualization of various breast tissue features of pathological importance and their correlations with histology revealed the potential of this multimodal nonlinear optical imaging technique for further clinical translation and cancer studies.

3.1 Basic tissue features

Through highlighting the targeted structural and molecular substances and displaying them in different color channels (Table 3.1), various basic tissue features were characterized in intraoperative label-free multi-contrast nonlinear optical images. Since these tissue features are distributed throughout the human breast tissues and play essential roles in various tissue events, the visualization and characterization of these established a comprehensive understanding of the optical signatures of human breast tissue that appeared in the nonlinear optical image data.

Human tissue was obtained and imaged intraoperatively under a protocol approved by the

institutional review boards at the University of Illinois at Urbana-Champaign and Carle Foundation Hospital. For the results discussed in this section, there were a total of eight imaging sites on seven breast tissue specimens excised from six human subjects by the surgeons during the breast cancer surgeries.

Table 3.1 Targeted substance and display of four imaging modalities

Imaging modality	Targeted substance	Display color
THG	Optical heterogeneity	Magenta
3PF	NADH	Cyan
SHG	Periodic structure	Green
2PF	FAD, elastin	Yellow

3.1.1 Adipocytes

Adipocytes were visualized in multi-contrast nonlinear optical images by the nonlinear optical signals generated from their inner contents and boundaries. As an inner content of adipocytes, NADH was highlighted in the 3PF imaging modality [6], and the optical heterogeneity at the boundaries of the adipocytes provided good phase-matching conditions for THG [13]. A group of nonlinear optical images of adipocytes together with a histological image is shown in Figure 3.2. The THG-contrast image in

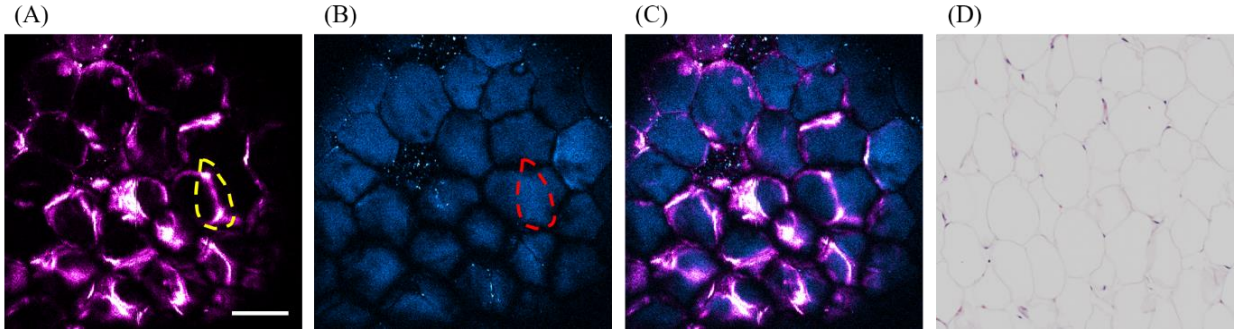

Figure 3.2 Multi-contrast images of adipocytes. (A) A magenta-colored THG image highlights the boundaries of adipocytes, while their inner contents are visible in a (B) 3PF-contrast image. When combined, most THG signals from the interfaces are well-aligned with the narrow gaps between the adipocytes in the 3PF-contarst image, which is presented in (C). Yellow-dashed circle in (A) marks the boundary between adipocytes that exists in the THG-contrast image but is absent in the 3PF-contrast image at the same location (red dashed circle in (B)). (D) Histological image of adipocytes. Scale bar: 100 μm.

Figure 3.2 (A) highlights the presence of adipocyte boundaries, and in Figure 3.2 (B), 3PF signals are mainly generated from inside the adipocytes. Notably, there were small dark gaps between adipocytes cells that were generally tightly grouped together. After combining these two different contrasted images together, the dual-contrast image is shown in Figure 3.2 (C). As expected, interfaces highlighted by THG match well with the small dark gaps in the 3PF-contrast image. However, some lipid boundaries are only identified from the THG-contrast image. In Figure 3.2 (A), the yellow-dashed line encircles a part of the interfaces between two adipocytes, while in the 3PF-contrast image, no discontinuity is identified from the same region inside the red-dashed circle. Given that the difference between the lateral resolutions of these two imaging modalities is relatively small (Section 2.4.1), it is the different nonlinear optical interactions behind THG and 3PF that produce this result. While 3PF depends on the concentration of fluorophores, THG is sensitive to the subtle spatial variations of optical properties, such as refractive index and higher order optical susceptibilities. Under the similar lateral resolution, 3PF cannot resolve the subtle discontinuity of concentration, but the THG signal can still be generated because of the good phase-matching condition created by the adipocyte interfaces [15]. This advantage of THG made it exceptionally suitable for EV visualization. One of the most notable difficulties in observing EVs is their small nano-scale size, which limits the cargo volume inside the EV and often yields a low image contrast from the inner content concentration. However, since all EVs have a membrane (unilayer or bilayer), strong THG signals were generated from these membrane interfaces. Therefore, THG imaging was used as a more sensitive way of detecting these extremely small EVs, which will be discussed in the next chapter.

3.1.2 Fibrous structures

The fibrous structure is another important feature in human breast tissue. Two major types of fibers are commonly visualized using nonlinear optical imaging: type I collagen fiber [35] and elastin fiber (Figure 3.3 [38]). Type I collagen fiber is commonly found in most connective tissues and plays an

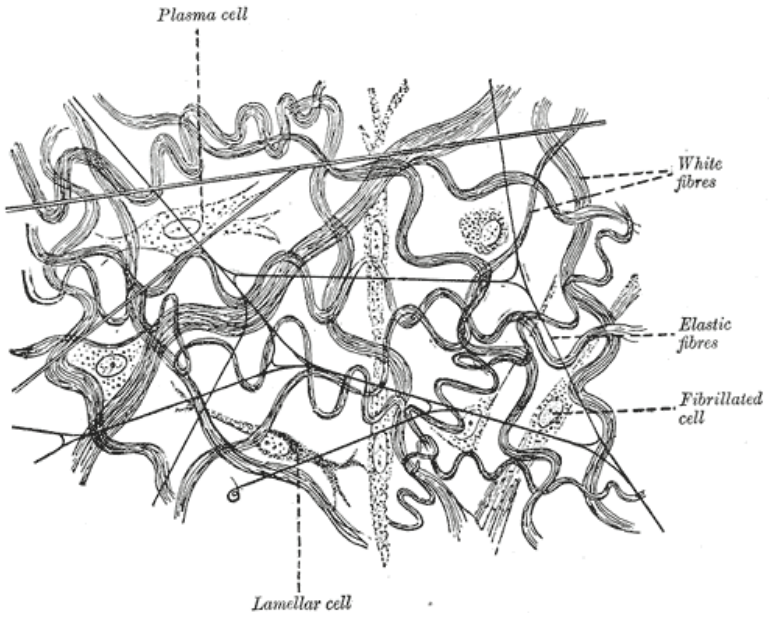

Figure 3.3 Diagram of collagen fibers and elastin fibers. The collagen fibers are thick and labeled as "white fibres", while the elastin fibers are much thinner [38].

essential role in sustaining tissue structures via formation of the extracellular matrix (ECM) [35]. ECM provides stable support for individual cells and cell groups to prevent them from flowing around the human body, and new growth of blood vessels can only take place with the firmness and integrity offered by the collagen fiber ECM. Therefore, rapidly growing and metastatic cancer cells also have considerable interactions with the ECM in human breast tissues, which results in different TACS identified in tumor tissues [36]. Elastin fiber, a rarer type of fibrous structure than collagen fibers, basically gives tissue the ability to return to its original shape after being stretched or pressed. In human breast tissue, the multi-contrast nonlinear optical imaging data revealed a trend that elastin fibers were found in more abundance in healthy breast tissues than in cancerous breast tissues.

Although Type I collagen fiber and elastin fiber are both biological fibers, the nonlinear optical signatures from each are entirely different. In this imaging system, elastin fibers normally generated strong 2PF signals simply due to the contained autofluorescent elastin protein. Type I collagen fibers, however, do not have a strong fluorescence response, and were typically visualized by SHG imaging because of their fibrillar structure. Notably, among the several types of collagen in human tissue, only

type I and type II collagen possess the suitable fibrillar structure that provides SHG imaging contrast, while type III and type IV are basically invisible in SHG images [10]. SHG, like another structural imaging modality THG, is generated from certain tissue structures with a special phase-matching condition. While the phase-matching condition for THG imaging is satisfied within one Rayleigh distance from any interface [13], periodic structures with a wavelength-level spatial period create a quasi-phase matching condition for SHG [37]. In breast tissues, collagen fibers (referred to as the type I collagen, same for below) have the favored periodic structure to generate a SHG signal in both the forward and backward directions. As is noticed in Figure 3.3 [38] and the "SHG" column of Figure 3.4, collagen fibers are relatively thick, which, from a microscopic perspective, results from the fact that each thick collagen fiber is a bundle of a larger number of thinner collagen fibers. Because of the difference of optical properties between collagen protein and water, these thick collagen fiber bundles form optically periodic structures. In the backward direction, the phase matching condition is achieved with the help of the axial momentum K_b provided by the periodic structure, which can also be treated as a grating wave vector. Taken into consideration, the grating wave vector K_b phase matching equation for the backward SHG signal can be expressed as

$$\Delta k_b = K_b - (k_{2\omega} + 2k_{\omega}). \tag{3.1}$$

It was found that the forward-directed SHG is predominant when the spatial periods formed by the collagen diameters are comparable to the wavelength of the SHG signal λ_{SHG} , and the percentage of the backward-directed SHG starts to reach 50% when the spatial periods of the collagen fibers are on the order of $\lambda_{SHG}/10$ [37].

The two entirely different imaging contrast mechanisms discriminate these two types of fibrous structures by the different nonlinear optical imaging modalities, instead of by their morphology as in histology. In Figure 3.4, four groups of SHG-2PF dual-contrast images are shown to highlight the differences between healthy and cancerous breast tissues in terms of features extracted from the fibrous

structures. In Figure 3.4 (A), images of healthy breast connective tissue are shown. The collagen fibers in the SHG-contrast image appear somewhat curvy, but are still toward an overall upper-right direction marked by a red arrow. In the 2PF-contrast image from the same site, a few elastin fibers can be identified with the features, including smaller diameters, sparser distribution, a more co-linear style of alignment, and a similar general direction of alignment (red arrow). In the composite image of SHG and 2PF, it is obvious that collagen fibers and elastin fibers are aligned toward approximately the same direction, and some of them are even strictly overlapping with one another. Because both kinds of fibers are essential components to connect different parts of the human body, this finding indicates the approximate position and orientation of this connective tissue in the human breast. The 2PF- and SHG-contrast images in Figure 3.4 (B) were also acquired from healthy breast tissue, but more structures are present in these images compared to other connective tissues. There is a dark region in the upper-right corner of both the SHG- and the 2PF-contrast images, which is surrounded by dense collagen and elastin fibers. According to the pathological interpretation, this dark area surrounded by fibrous structures represents a mammary duct, through which milk passes. The patient in this case was relatively young at age 45, possibly retaining more functional activity in the breast compared to older patients. In the 2PF-contrast image, many radially aligned elastin fibers, marked by the red arrows, are distributed around the mammary ducts, which come from the boundary of the mammary duct and extend outward in various directions. It is very likely that these radially aligned elastin fibers were there to help retain the shape of the duct. In cancerous tissues, however, these radially aligned elastin fiber structures near the mammary ducts were absent, as shown in Figure 3.4 (C). Specifically, for 2PF- and SHG-contrast images collected from a site inside a breast tumor (Figure 3.4 (D)), virtually no elastin fibers can be found inside the tumor area. 2PF signals mainly highlight cells and some adipocytes with a 2PF response. The SHG-contrast image in Figure 3.4 (D) clearly shows the tumor-induced collagen realignment. In the lower half of the image FOV, collagen fibers are more sparsely distributed than in the two images collected from healthy connective tissues, and are randomly aligned with no dominant direction, creating small chambers for the groups of tumor cells.

In conclusion, by observing and analyzing the characteristics of fibrous structures visualized

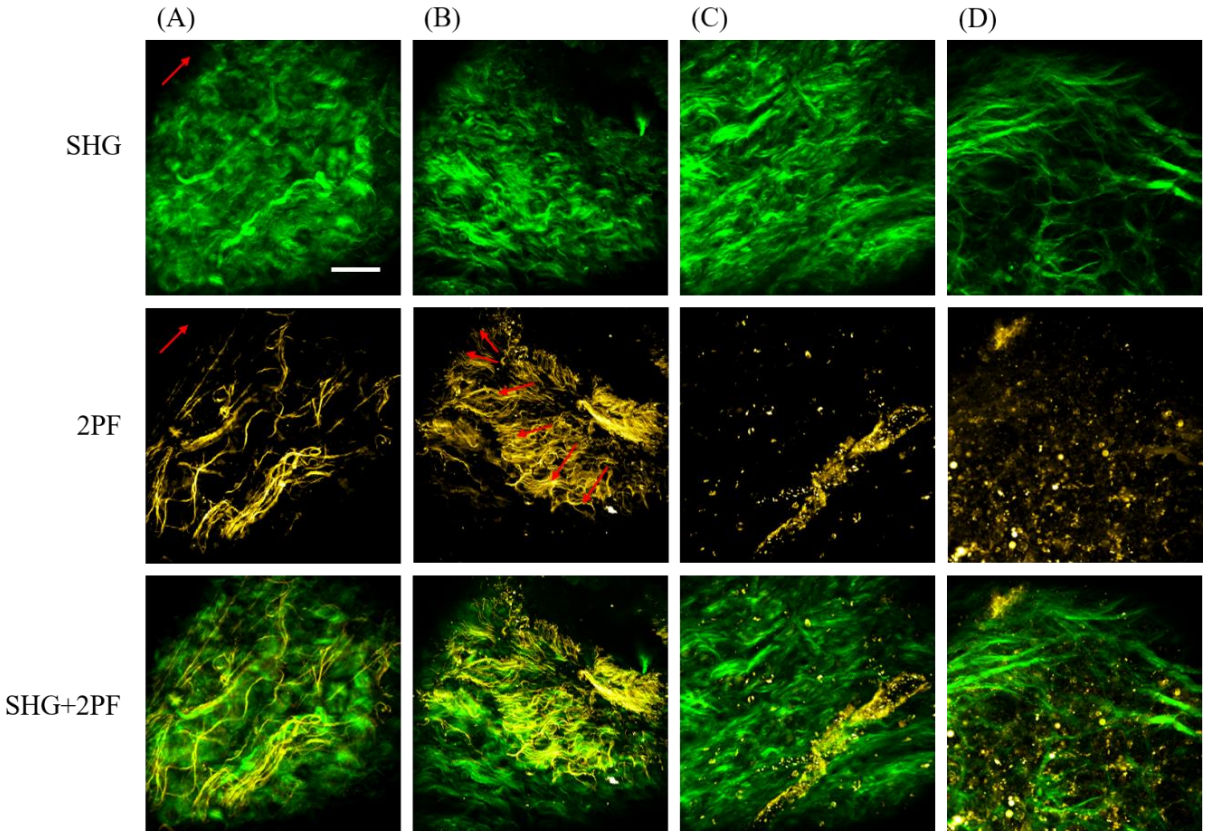

Figure 3.4 Nonlinear optical images of collagen fibers and elastin fibers in human breast tissues. SHG-contrast images in green are displayed in the first row labeled "SHG", and 2PF-contrast images in yellow are shown in the second row labeled "2PF". Dual-contrast images combining the first and second rows are shown in the third row. Images in column (A) are from a healthy breast connective tissue site, with red arrows marking the overall direction of fiber alignment. Images in column (B) highlight collagen and elastic fibers near a mammary duct in healthy breast tissue. Red arrows show the radial elastin fibers around the mammary duct, which cannot be found near mammary ducts in cancerous tissues shown in column (C). Column (D) includes images acquired inside a tumor. Collagen fibers have a very different alignment compared to the first two columns and no elastic fibers are identified. Scale bar: 100 µm.

primarily by 2PF and SHG, such as their diameter, space, location, and alignment, essential information about human breast tissues was extracted to differentiate tissue types, identify tissue structures like mammary ducts, and locate tumor areas.

3.1.3 Cells

Cells are the most essential structures in breast tissues for pathological cancer diagnosis. By examining the size, shape, distribution, and nuclear properties of cells, pathologists can distinguish malignant cells from pre-malignant or benign cells in metaplasia and hyperplasia. In H&E-stained histology, cells typically have pink cytoplasm and dark-colored nuclei. However, using the four label-free

imaging modalities in this system, cell nuclei were found to lack any structural phase-matching condition and any molecule with strong autofluorescence, meaning that cell nuclei did not provide any observable nonlinear optical signal, making it hard to use the standard nuclear features to diagnose cancer in the label-free multi-contrast nonlinear optical images. Therefore, cells were identified in multi-contrast nonlinear optical images primarily by the visible cytoplasm and the dark nuclei.

Figure 3.5 includes the multi-contrast nonlinear optical images of different types of cells with the co-located histological images. An essential way to differentiate cell types is by their shapes, which can be performed by either the nonlinear optical images or the histological images. For instance, endothelial cells from a blood vessel usually have a narrow and elongated shape, while tumor cells normally appear round and small. In addition, multimodal nonlinear optical imaging provides a unique contrast of cells that is lacking in conventional H&E-stained histological images: nonlinear optical signatures of the cell

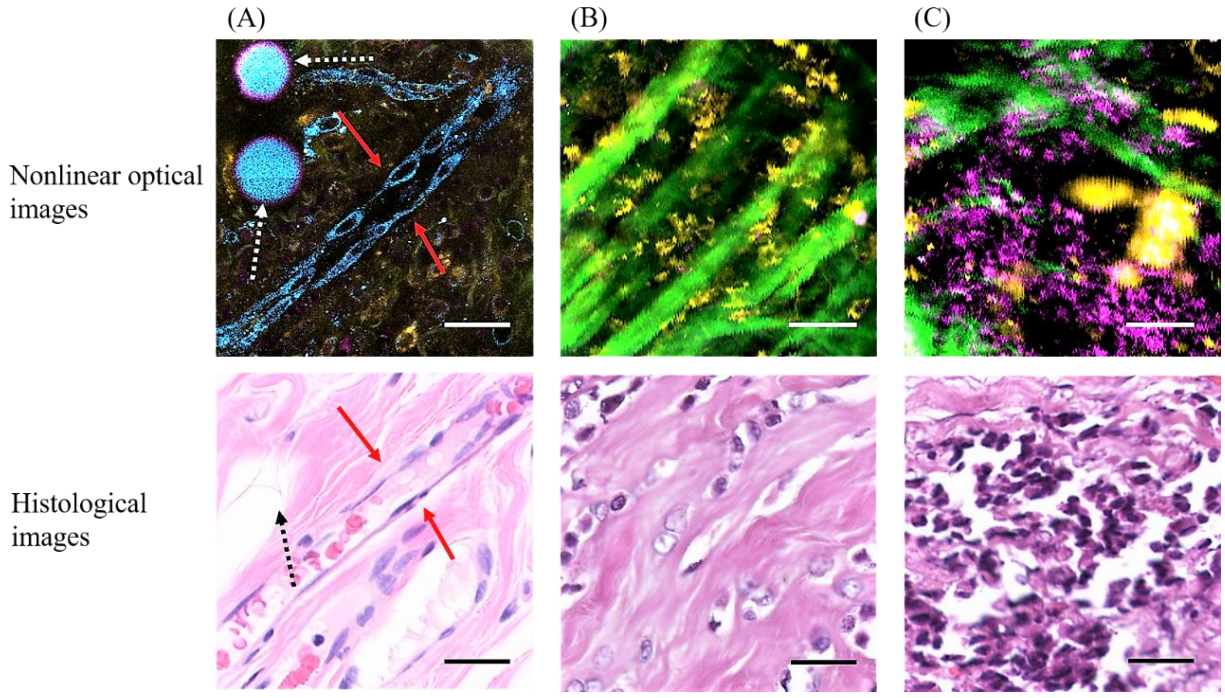

Figure 3.5 Multi-contrast nonlinear optical images and histological images of cells. (A) Endothelial cells form a blood vessel, which was highlighted by 3PF-contrast of the cytoplasm in the nonlinear optical image. White and black dashed arrows mark the adipocytes and red arrows point at endothelia cells in a blood vessel [6]. (B) Small groups of stromal cells and tumor cells were surrounded by dense extracellular matrix. Yellow signals are generated from the cytoplasm via 2PF. (C) Large groups of malignant tumor cells, which was visualized by THG-intense cytoplasm and dark nuclei. Scale bar: 50 μm.

cytoplasm. As illustrated in Section 2.3.4, the metabolic chemical components FAD and NADH, as well as other autofluorescent molecules, are present in many cells and can be respectively visualized in 2PF- and 3PF-contrast images. Therefore, 2PF and 3PF signals provide extra molecular contrast to cells. For example, the endothelial cells in the nonlinear optical image of Figure 3.5 (A) have a 3PF-visible cyan cytoplasm, while the cytoplasm of stromal and tumor cells in Figure 3.5 (B) generate strong 2PF signals in yellow. Other than the molecular information from 2PF and 3PF, structural information of cells can also be visualized by the multimodal imaging system via THG. Membrane structures like EVs and ribosome are exceptionally abundant in certain groups of cells, which is the case for the cells from invasive lobular carcinoma shown in Figure 3.5 (C). Tumor cells in the nonlinear optical image of Figure 3.5 (C) are featured by the THG-visible cytoplasm likely caused by the EV formation inside these tumor cells.

To sum up, this nonlinear optical imaging demonstrates new contrast mechanisms for visualizing and differentiating different types of cells. These molecular and structural contrasts provide essential information about cell metabolism and other activities, which can be used to study cancer invasion and provide new tools for cancer pathology.

3.1.4 Mammary lobules

Mammary lobules, completely benign structures in the tumor microenvironments, have been recognized in intraoperative image data by comparing with histology. Mammary lobules are a special type of gland that produces milk in nursing women. They are usually connected to the nipple by a mammary duct to transport milk. Because of their functions, mammary lobules and ducts share similar tissue structures and components: The cavities and lumens of mammary lobules and ducts are normally enclosed by epithelial cells, which are surrounded by some collagen and elastin fibers.

In Figure 3.6 (A), some circularly shaped collagen fibers appear in the green-colored SHG channel surrounding small groups of cells and possibly some elastic fibers visualized by the 2PF signal, which is perfectly correlated with the histological image acquired from the same location (Figure 3.6 (B)).

In addition, strong 2PF signals were also generated outside these lobules in Figure 3.6 (A). In this circular region of intense 2PF signal, there are a few cell-like structures indicated by the red arrows. In the histological image (Figure 3.6 (B)), a thin layer of cells around the normal lobules is identified and some of the cells are marked with the red arrows. Therefore, compared with the histological image, the circular region of intense 2PF signal surrounding the lobules in Figure 3.6 (A) probably originates from the cytoplasm of this cell layer in the histological image. The ambiguity of cells in the nonlinear optical image was most likely caused by the motion-induced image jitter, the signal saturation, and the overlapping of cell cytoplasm that is substantially lost in the histological image because of the tissue preparation.

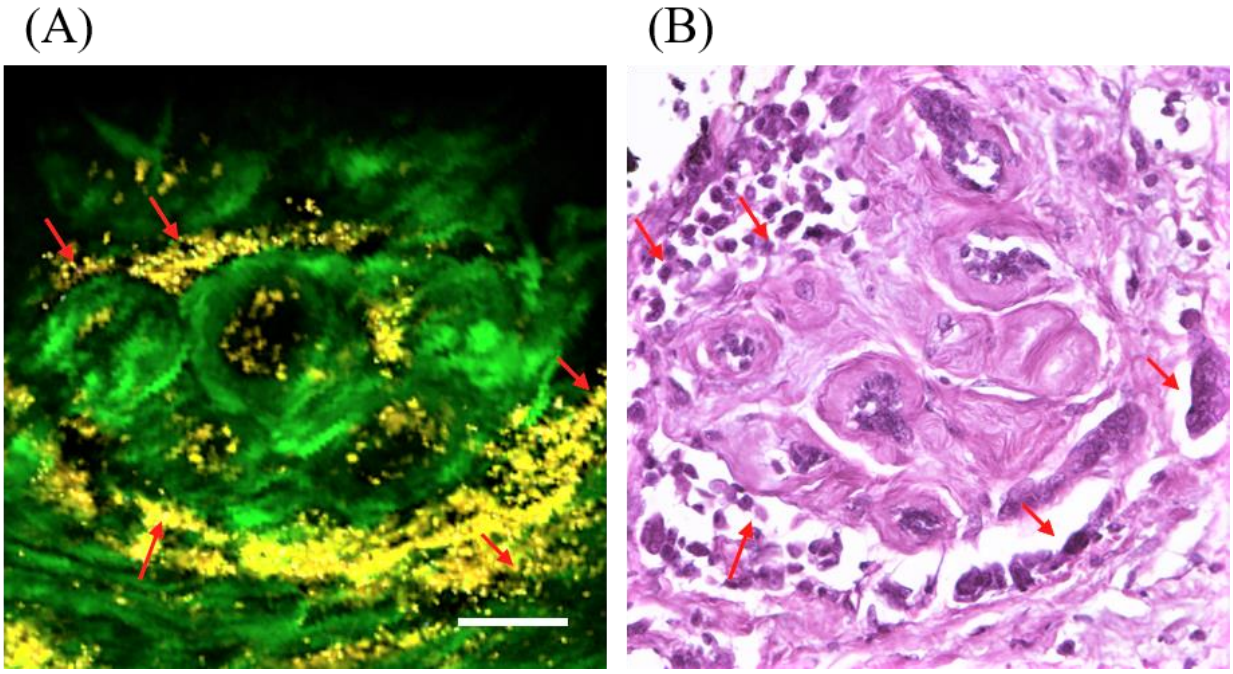

Figure 3.6 (A) Multi-contrast nonlinear optical image and (B) the co-located histological image of mammary lobules. Red arrows indicate the cells surrounding the lobules. Scale bar: 50 µm.

3.2 Differentiation of breast tumor subtypes

Based on these basic tissue features identified and characterized from multi-contrast nonlinear optical images, more challenging clinical applications were attempted using the intraoperative imaging system. Three major subtypes of human breast tumor were visualized in multi-contrast nonlinear optical images. By comparing with histology slides collected from the same tissue site, some tissue features used

to define and differentiate breast tumor subtypes in histopathology, like the tumor-associated collagen fiber signatures (TACS) and the characteristics of tumor cells, were recognized in multi-contrast nonlinear optical images as well. These correlations between the nonlinear optical images and the related histological images helped characterize these intraoperatively visualized tumor subtypes and provide evidence to differentiate them by nonlinear optical imaging modalities.

Human tissue was obtained and imaged intraoperatively under a protocol approved by the institutional review boards at the University of Illinois at Urbana-Champaign and Carle Foundation Hospital. For the results discussed in this section, five images were acquired from five imaging sites on three breast tissue specimens excised from three human subjects by the surgeons during the breast cancer surgeries.

3.2.1 Invasive ductal carcinoma (IDC)

As the most common subtype of invasive carcinoma in breast tissue, IDC typically originates from the endothelial cells of mammary ducts. IDC is characterized in histopathology by thick rows composed of large groups of tumor cells that are aligned along a similar direction [39]. In the multi-contrast nonlinear optical images (Figure 3.7 (A)), tumor cells are also gathered in large numbers, constructing a nest-like structure with an overall orientation marked by red arrows in Figure 3.7 (A). These cells are distinguished by their yellow or magenta cytoplasm, which separately represent the 2PF and THG signals. In addition, the collagen fibers, shown in the green channel in Figure 3.7 (A), are approximately aligned in the same direction in response to tumor cell infiltration, as verified by the histological images shown in Figure 3.7 (B).

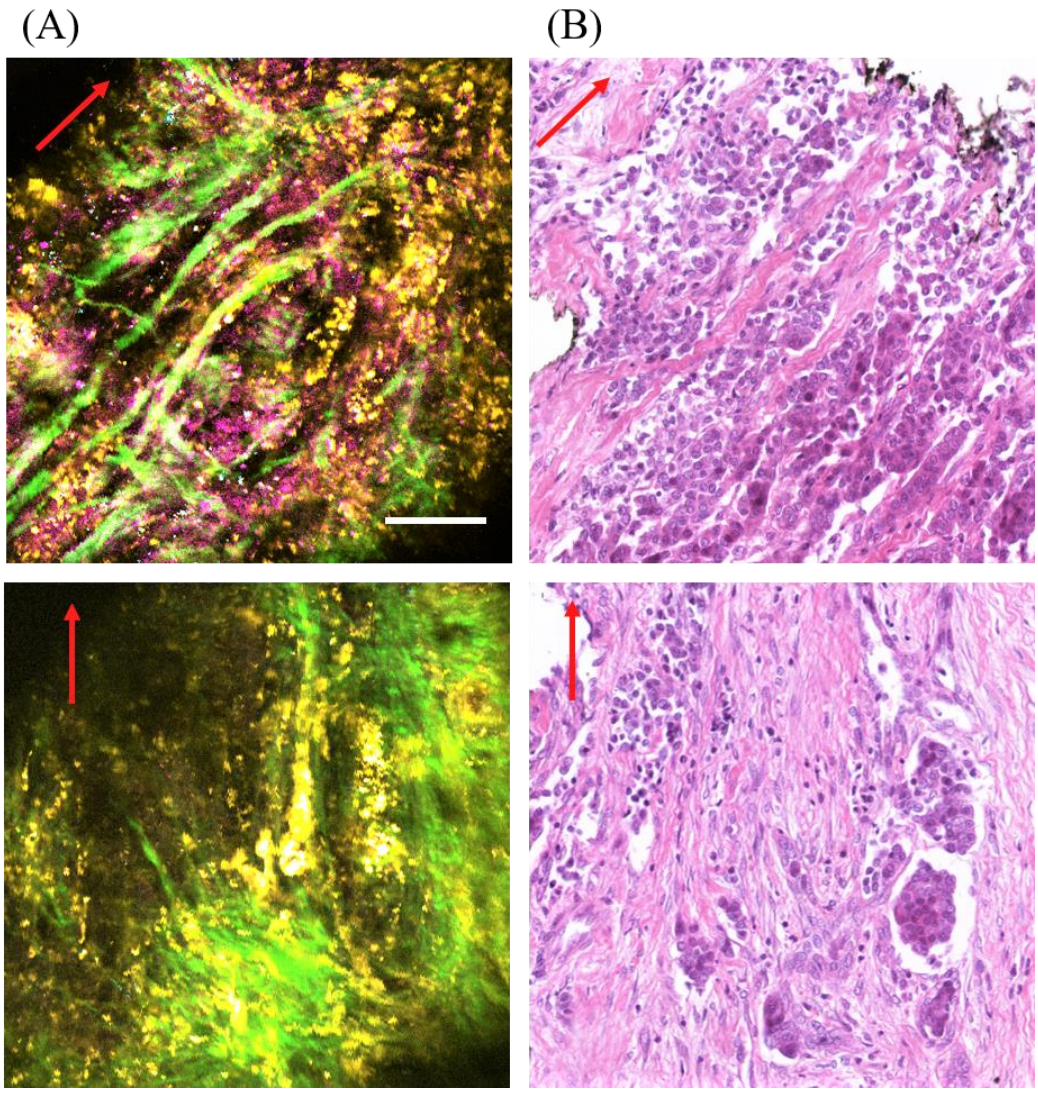

Figure 3.7 (A) Multi-contrast nonlinear optical images and (B) the co-located histological images of invasive ducat carcinoma (IDC). Red arrows indicate the orientation of the tumor cell organizing pattern. Scale bar: 100 µm.

3.2.2 Invasive lobular carcinoma (ILC)

Invasive lobular carcinoma (ILC) is the second most common subtype of breast tumor. The histology of ILC is identified by the small rows of infiltrating tumor cells with a width of one or two cells per row [40]. Moreover, the tumor cells of ILC typically are poorly cohesive, small and monomorphic, with less cytoplasm than IDC [40]. Figure 3.8 shows the nonlinear optical images and histological images acquired from two sites on a specimen of breast tissue with ILC. The tumor cells visualized by the 2PF imaging modality are recognized by the yellow cytoplasm and dark nuclei in Figure 3.8 (A). In the first

row of Figure 3.8, both images show that tumor cells are aligned in rows within two cells wide and surrounded by realigned collagen fibers. However, it is difficult to recognize these rows because of the randomness of the row orientations as well as the dense distribution. In contrast, the images in the second row of Figure 3.8 present a clear alignment of both tumor cell rows and collagen fibers. Compared with the large cell groups in IDC (Figure 3.7), the tumor cells in ILC were found to be organized in much narrower rows, which have been rigorously interpreted from the histological images as well as the multi-contrast nonlinear optical images.

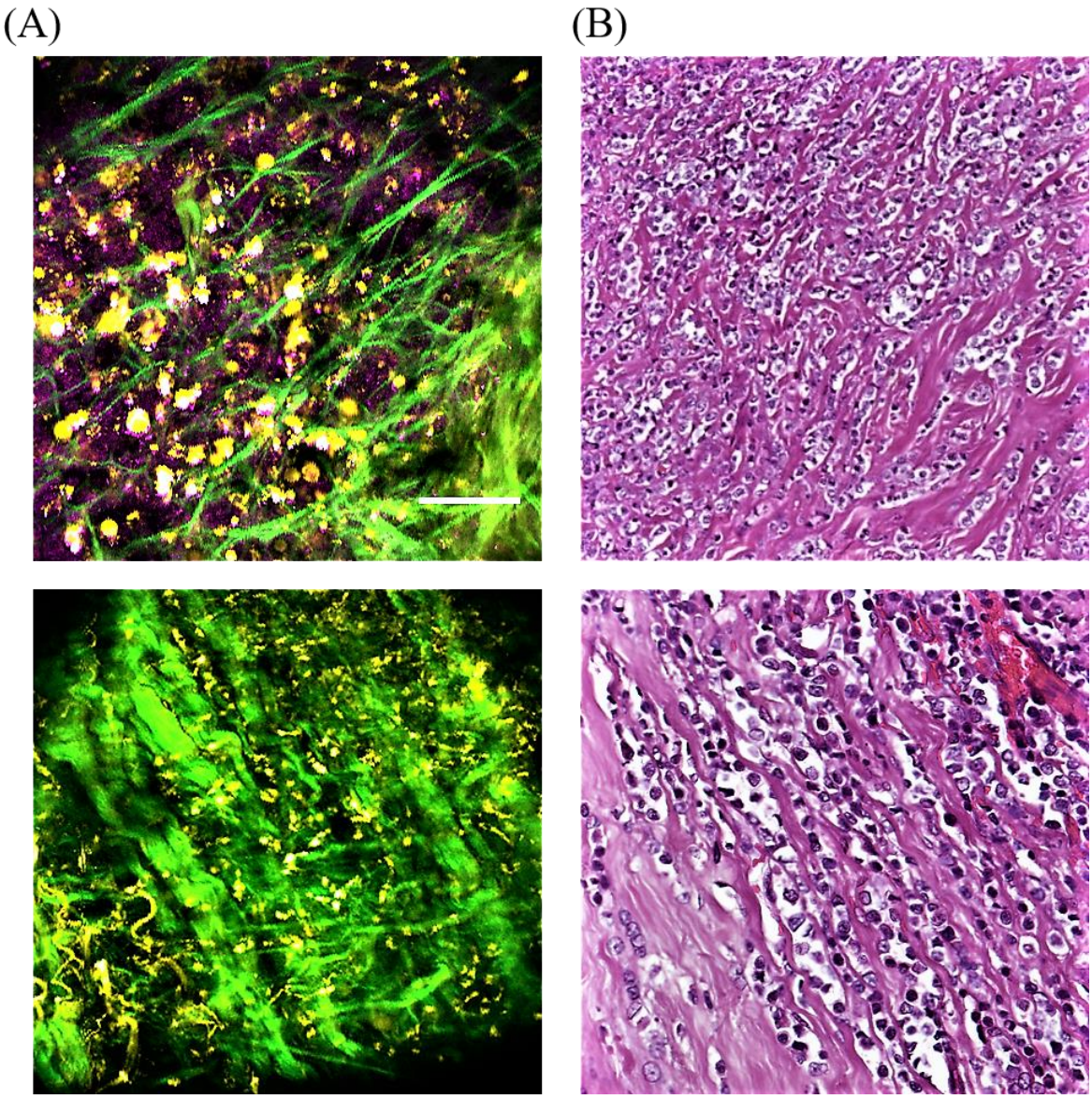

Figure 3.8 (A) Multi-contrast nonlinear optical images and (B) the co-located histological images of invasive lobular carcinoma (ILC). Scale bar: 100 μm.

3.2.3 Invasive micro-papillary carcinoma (ImPC)

Invasive micro-papillary carcinoma (ImPC) is a rare breast tumor subtype. Different from the two subtypes discussed above, ImPC has smaller-sized tumor cells gathered in large numbers with surrounding clear spaces [41]. In Figure 3.9, the small tumor cells highlighted by the strong THG signal in the nonlinear optical image are gathered in several larger unorganized regions (outlined by yellow dashed lines) that are loosely separated from each other by a few sparsely distributed collagen fibers. Unlike IDC and ILC, these groups of cells in ImPC do not share a similar morphological shape, such as the rows in IDC and ILC. Although the surrounding clear spaces of ImPC are not present in the limited FOV of this image, there is other evidence found in the multi-contrast nonlinear optical images that can be used to differentiate this tissue site from IDC and ILC, such as the small tumor cells, the tumor cell aggregation of random shapes, and the sparsely distributed collagen fibers.

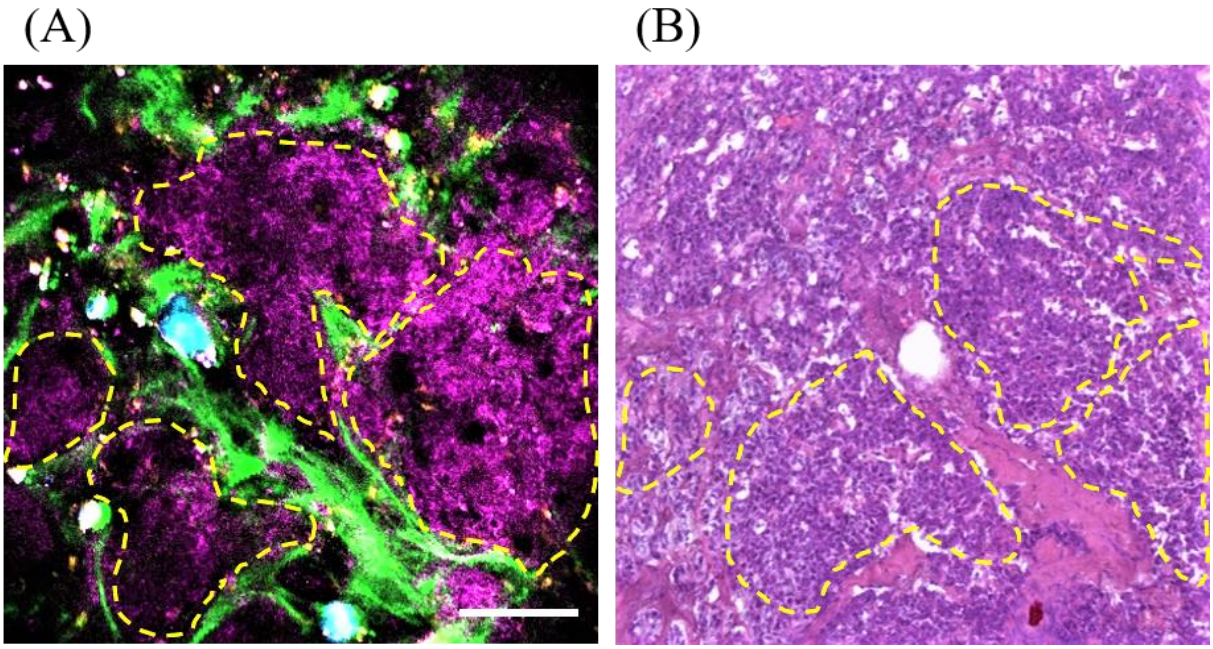

Figure 3.9 (A) Multi-contrast nonlinear optical image and (B) the co-located histological image of invasive micropapillary carcinoma (ImPC). Yellow dashed lines encircle groups of tumor cells. Scale bar: 100 µm.

3.3 Activities and events in tumor microenvironments

In addition to breast tumor subtypes, important tissue events occurring within the tumor microenvironment were also visualized by the intraoperative nonlinear optical imaging system. Nonlinear optical characterization of these events was realized by comparing the acquired images with

co-located histological images. Together, these contributed to the comprehensive interpretation of the nonlinear optical signatures of the tumor microenvironment.

Human tissue was obtained and imaged intraoperatively under a protocol approved by the institutional review boards at the University of Illinois at Urbana-Champaign and Carle Foundation Hospital. For the results discussed in this section, five images were acquired from five imaging sites on three specimens of breast tissue excised from three human subjects by the surgeons during the breast cancer surgeries.

3.3.1 Desmoplastic reaction

Desmoplastic reaction, or desmoplasia, is a pathophysiologic event occurring in the stroma of a breast tumor, and is commonly used to analyze cancer invasion [42-45]. Using the intraoperative imaging system, multi-contrast nonlinear optical images were captured at two tissue sites in the tumor microenvironment of a specimen of breast tumor tissue. These sites were recognized by a board-certified pathologist as containing desmoplastic reaction using the co-located histological images. The nonlinear optical signatures associated with the cancer invasion stage were identified and validated by comparing images with the co-located histological images.

In Figure 3.10 (A) and (B), some dense and thick collagen fibers are located below the red dashed line, which is recognized as the desmoplastic region. In addition, cells are mostly found above the red dashed line in both the nonlinear optical and histological images, which is the tumor region. In this imaging site, the collagen fibers in the desmoplastic region were tightly aligned, which leaves little space for tumor cell infiltration. That is because a desmoplastic reaction, at an early stage, is a secondary reaction of the human body trying to “heal” the tumor-like wound by producing dense fibrosis [45]. At this early stage, the tumor cells inside the tumor region had not started to invade this dense ECM. However, it is still unknown whether this reaction is actively initiated by the tumor or just a passive reaction from the body. Nevertheless, this imaging site can be attributed to an early invasive stage based

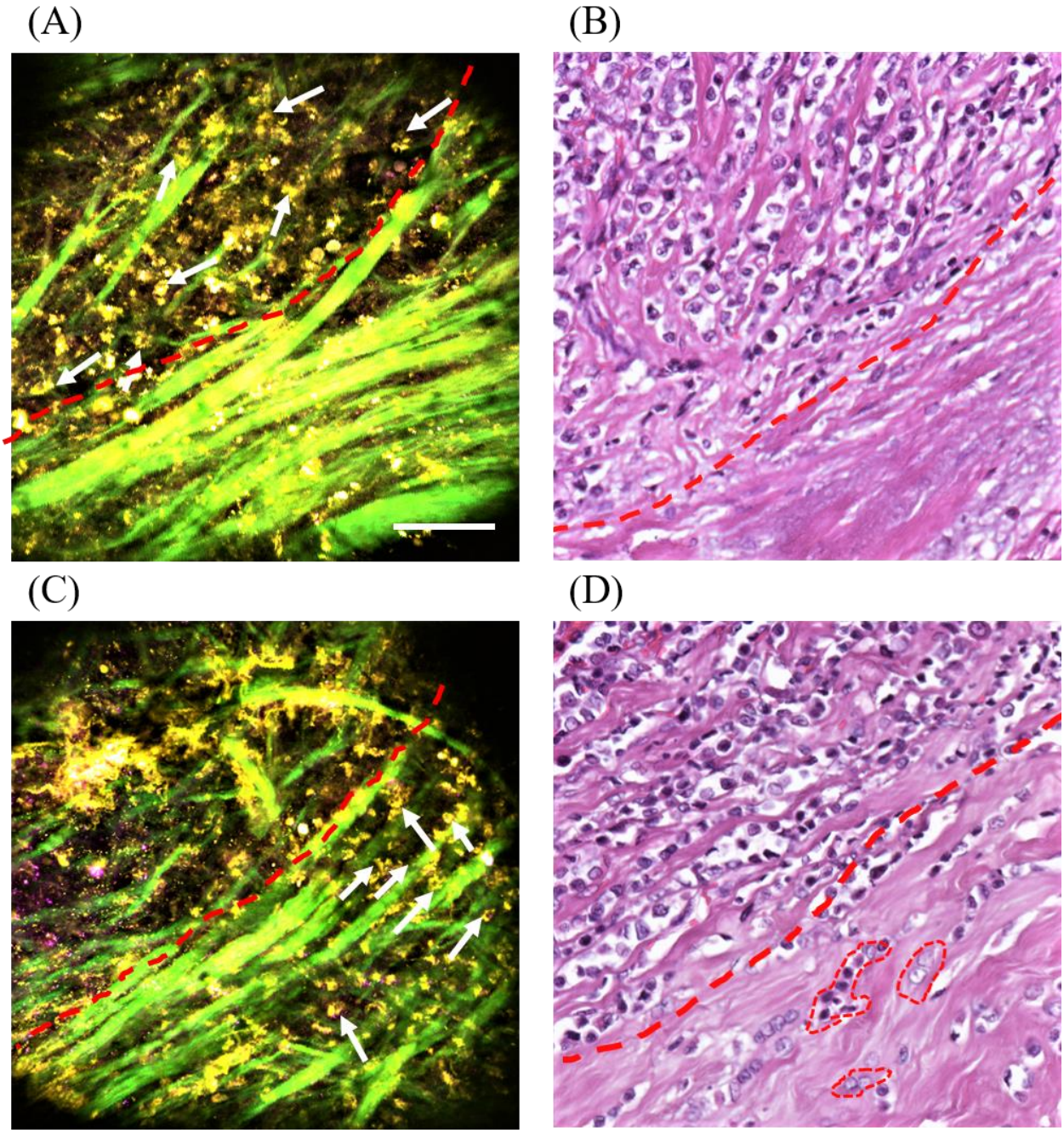

Figure 3.10 Images acquired from sites of desmoplastic reaction. (A) Multi-contrast nonlinear optical image of desmoplasia at an early stage. The red dashed line marks the interface between tumor and the dense collagen fibers of the desmoplastic reaction, and tumor cells are identified only in the tumor region (white arrows). (B) Histological image collected at the same site of early-stage desmoplastic reaction, with the red dashed line marking the tumor-desmoplasia interface. (C) Multi-contrast nonlinear optical image of desmoplasia at a later stage. The red dashed line marks the interface, with infiltrating tumor cells found within the collagen region (white arrows). (D) Histological image collected at the same site of the late-stage desmoplastic reaction, with the red dashed line marking the tumor-desmoplasia interface and red dashed contours encircling infiltrating tumor cells. Scale bar: 100 μm.

on these morphological features interpreted from both images, such as the dense and thick collagen fibers and the lack of cells within the desmoplastic region.

Later stages of tumor invasion near sites of desmoplasia are initiated by the secretion of ECM degrading enzymes like matrix metalloproteinases (MMPs) from tumor cells [46], which can break down and remodel the dense collagen fibers produced by the desmoplastic reaction, and use these fibers as a scaffold to accommodate the further infiltration of tumor cells. In Figure 3.10 (C) and (D), small gaps are evident between the desmoplasia-associated collagen fibers below the red dashed line, and a few groups of cells (white arrows in Figure 3.10 (C) and red dashed contours in Figure 3.10 (D)) are identified within these gaps. In the breast tumor histopathology, the presence of tumor cells inside the new ECM normally signifies a later stage of local tumor invasion [46]. Moreover, as identified in the histological image (Figure 3.10 (D)), some active fibroblasts that are probably induced by tumor-stroma interactions are located adjacent to the infiltrating tumor cells, which are found to play an essential role of aiding tumor invasion by producing more collagen fibers for the scaffold [47].

There were several similarities between these two imaging sites in breast tumor tissue. First, both original tumor regions were located at the upper left part of the FOV, and the desmoplasia-associated collagen fibers were identified in the lower right. Second, these dense, thick, and straightened desmoplasia-associated collagen fibers can be easily distinguished from the thin and wavy ones within the tumor regions. Third, the boundaries of the desmoplastic reaction were clearly visualized and marked in all four images. These similarities helped classify both sites as the desmoplastic reaction and enabled the direct comparison between them in terms of invasion stage. As mentioned above, Figure 3.10 (A) and (B) present an early stage of tumor invasion because of the dense collagen and the lack of cells inside the desmoplasia-associated ECM. In Figure 3.10 (C) and (D), however, gaps and cells between desmoplasia-associated collagen fibers indicate a later and more aggressive stage of tumor invasion.

3.3.2 Apocrine metaplasia

Apocrine metaplasia in the human breast is generally a benign breast condition that is considered to be associated with various fibrocystic breast changes [48]. Although named as “apocrine”, it is related not to sweat glands but often to mammary lobules and ducts. In tissue sites with apocrine metaplasia, epithelial cells of mammary ducts or lobules present with an altered appearance under histology, and a growing number of cells inside ducts or lobules are reported in some cases [48]. Although cell growth of apocrine metaplasia is strictly controlled, and thus different from the proliferation of carcinoma *in situ*, apocrine metaplasia shares similar features with carcinoma under conventional medical imaging like X-ray or ultrasound [49]. Therefore, it is difficult for doctors to completely rule out the possibility of carcinoma with the presence of apocrine metaplasia in X-ray or ultrasound images, and often the biopsy is still necessary to reliably diagnose apocrine metaplasia [50].

Human breast tissue with apocrine metaplasia was imaged using the intraoperative nonlinear optical imaging system. Unique morphological features were found from multi-contrast nonlinear optical images, which yielded strong correlations with co-located histological images (Figure 3.11). It is clearly noticed in multi-contrast nonlinear optical images (Figure 3.11 (A) and (C)) that the 2PF signal reveals a tightly organized cellular structure, which highly resembles the cells of apocrine metaplasia in the related histological images. While cell nuclei are visualized in the histology, it is difficult to find the clear boundaries between each cell. Nonlinear optical images, however, show that these 2PF-intense cells are separated from their adjacent cells by clear boundaries. Additionally, the 2PF signal intensities of these cells are considerably higher than those of the tumor cells visualized in the multi-contrast nonlinear optical images, which means these metaplastic cells probably contained an exceptionally high concentration of FAD or other autofluorescent molecules in their cytoplasm. These unique optical features of apocrine metaplasia-associated cells in multi-contrast nonlinear optical images provide extra evidence for the application of diagnosing apocrine metaplasia. By using the nonlinear optical imaging as the imaging method for breast cancer biopsy after a suspicious X-ray or ultrasound result, physicians and patients would get a rapid diagnosis that could substantially reduce their anxiety during the waiting period

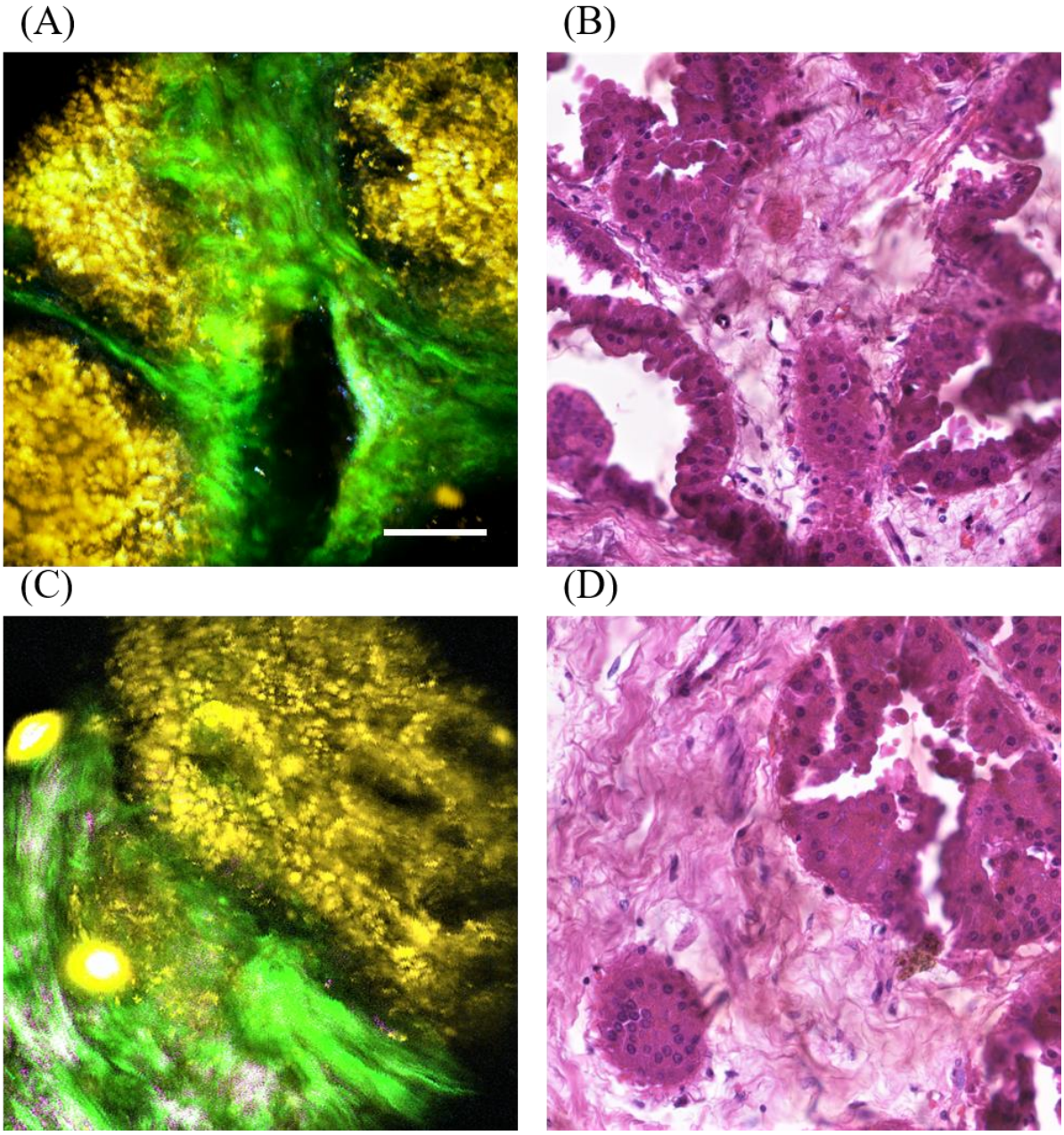

Figure 3.11 Images of apocrine metaplasia at two different sites. (A) Multi-contrast nonlinear optical images of apocrine metaplasia at the first site with (B) the co-located histological images. (C) Multi-contrast nonlinear optical images of apocrine metaplasia at the second site with its (D) co-located histological image. Scale bar: 100 μm.

required for the histology preparations.

Specifically, by examining the histological image from a larger FOV (Figure 3.12), cells are found to be grouped in papillae that show a tendency to contact each other within the lumen, which matches the definition of a complex papillary apocrine metaplasia (PAM) [48]. Patients with complex

PAM experience a relative risk of 1.2 to have subsequent carcinoma development [48]. Therefore, visualization of PAM by nonlinear optical imaging at a larger FOV would also assess the potential risk of developing breast carcinoma without time delay.

To sum up, the nonlinear optical imaging provides a promising tool for breast cancer biopsy by differentiating benign lesions from lesions suspicious for malignancy. As a result, in place of H&E stained histology, the fast and label-free nonlinear optical imaging of biopsy specimens would essentially reduce the labor and time cost, as well as the patients' anxiety.

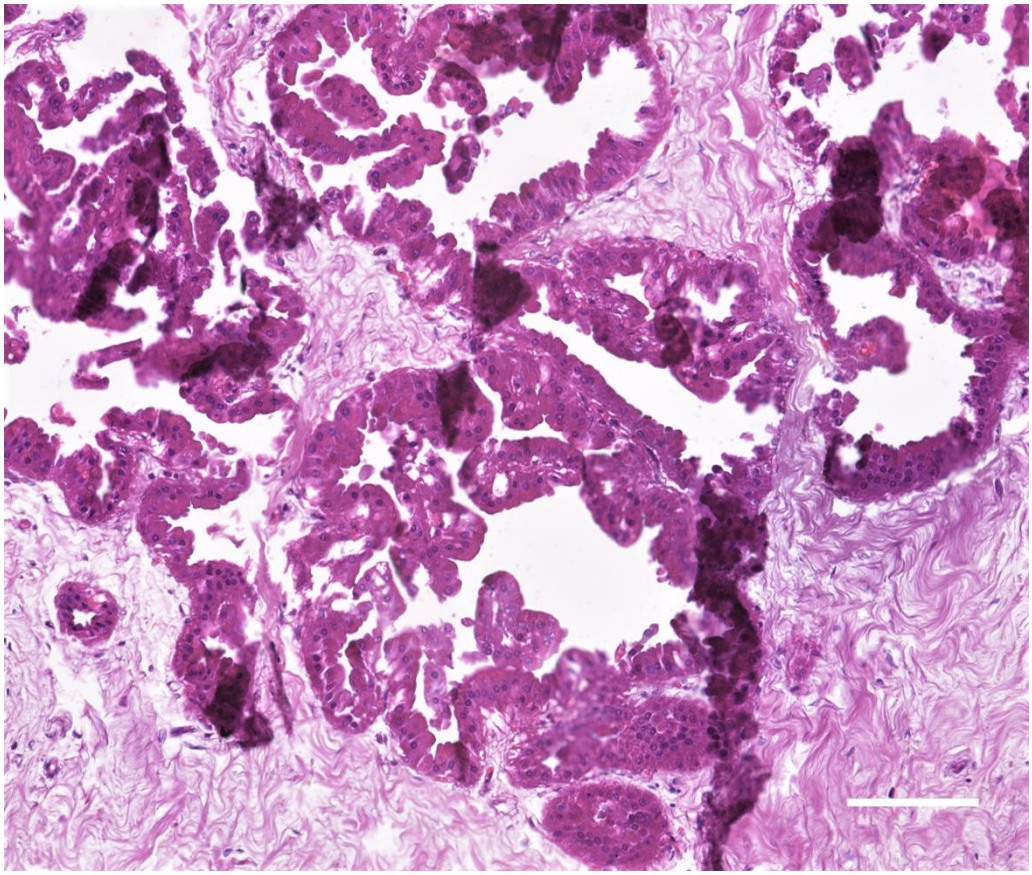

Figure 3.12 Histological image of apocrine metaplasia at a large FOV. Scale bar: 100 μm.

3.3.3 Radial scar

Radial scar is another feature in human breast that can be misleading in a mammogram. Biopsy is still considered mandatory to examine this kind of feature, although it can be potentially mistaken for tubular carcinoma in H&E stained histology [51]. In fact, compared to apocrine metaplasia, radial scars

are reported with a much higher chance of association with surrounding proliferating disease and malignancy, which often leads to surgical excision [52].

Radial scars in histology are usually characterized by a central fibroelastotic core containing entrapped glandular elements as well as the surrounding ducts and hyperplasic tissues radiating outward, which generate a stellate appearance [51]. The intraoperative imaging system captured a multi-contrast nonlinear optical image showing the core of a radial scar (Figure 3.13 (A)). Both the nonlinear optical and the co-located histological images (Figure 3.13 (B)) clearly visualized the curved elastin and collagen fibers within this central fibroelastostic core, but failed to provide contrast for the entrapped glandular elements. Different from benign radial scars, the central core of this radial scar is surrounded by the tumor cells of ImPC, which is shown in Figure 3.13. Therefore, supposing the tissue specimen were acquired in biopsy, the multimodal nonlinear optical imaging system would potentially be able to replace H&E stained histology to provide instant clinical guidance.

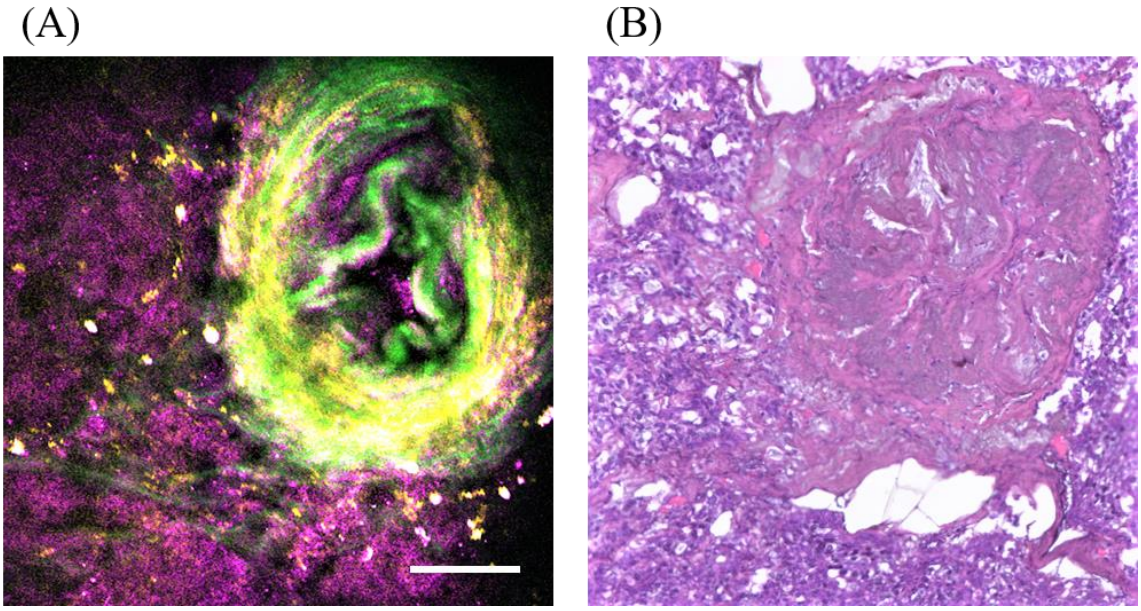

Figure 3.13 (A) Multi-contrast nonlinear optical and (B) co-located histological image of a central fibroelastotic core of a radial scar. Scale bar: 100 μm.

3.4 Summary

To sum up, various tissue features visualized by the intraoperative imaging system were present in this chapter, ranging from basic tissue structures to complicated tissue events. The credibility of the

nonlinear optical imaging modalities was proved through the comparison with co-located histological images acquired several days after the breast cancer surgery. Nonlinear optical signatures of basic features like adipocytes, fibrous structures, various types of cells, and mammary lobules were characterized to initiate the comprehensive database of nonlinear optical signature of the breast tumor microenvironment. Furthermore, as pioneer applications, some attempts were made to use the intraoperative imaging system to provide pathological guidance for tumor subtype differentiation, cancer invasion stage determination, and suspicious lesion verification, which revealed the potential of this intraoperative imaging technique for tumor microenvironment examination and even histopathology.

In addition to providing tissue information at the cellular level, the intraoperative imaging system also has the ability to visualize subcellular structures – the extracellular vesicles (EVs), which do not appear in histology preparations and have never been visualized intraoperatively before. The intraoperative visualization and quantification of EVs in the *ex vivo* breast tumor microenvironments are illustrated in the next chapter.

4 Quantification of extracellular vesicles (EVs) and correlations with pathological diagnosis

Visualization and quantification of EVs are first demonstrated in Section 4.2. Then, the following sections present the good correlations found between EV quantification results and pathological results, such as tissue type, distance from tumor region to closest margin, and the histological grade of invasive ductal carcinoma (IDC) and ductal carcinoma *in situ* (DCIS). Although the data analysis is based on a limited number of breast cancer and healthy breast reduction cases, these pathological correlations of EV quantification are highly significant for EV studies and for understanding tumor invasion mechanisms. In addition, the label-free EV image data highlights the potential for using EVs as a biomarker that can diagnose cancer in a fast, label-free and more accurate way.

Human tissue was obtained and imaged intraoperatively under a protocol approved by the institutional review boards at the University of Illinois at Urbana-Champaign and Carle Foundation Hospital. For the results discussed in this section, a total of 30 nonlinear optical images were acquired from 30 imaging sites on 19 tissue specimens from 19 breast cancer subjects, and 42 nonlinear optical images were acquired from 42 imaging sites on 10 healthy breast tissue specimens from 7 healthy subjects undergoing breast reduction surgeries. Table 4.1 summarizes the pathological information as well as the average and standard deviation of EV count quantified from images from these breast cancer cases.

Notably, either IDC or DCIS is lacking in certain cases, which are noted as “Not present” under invasion grade and “-” at the corresponding distance. In addition, some entries are filled with “Not specified”, meaning that the pathologists did not include this information in the pathology reports.

Table 4.1 Pathological and EV quantification data of imaged breast cancer cases

Surgery type	IDC grades	DCIS grades	Distance from closest IDC margin (mm)	Distance from closest DCIS margin (mm)	EV count
Mastectomy	Not present	Not present	-	-	5 ± 4
Mastectomy	2	Unspecified	1	8	26 ± 14
Mastectomy	1	Not present	6	-	13 ± 4
Mastectomy	1	Not present	1	-	15 ± 7
Lumpectomy	2	Not present	Not specified	-	18 ± 10
Lumpectomy	2	Not present	10	-	19 ± 9
Mastectomy	Not present	II	-	16	17
Lumpectomy	1	I	1	1	27
Mastectomy	1	II	2	5	13
Mastectomy	2	II	51	51	12
Mastectomy	2	II	14	17	15 ± 2
Lumpectomy	2	II	12	14	18
Lumpectomy	2	II	11	14	19
Mastectomy	2	II	10	10	23
Mastectomy	2	II	6	10	28
Lumpectomy	2	II	3	1	27 ± 15
Segmental mastectomy	2	III	1	Not specified	31
Mastectomy	3	III	5	positive	45
Mastectomy	3	III	10	10	25

4.1 Introduction and background

Extracellular vesicles, as a special kind of inter-cellular communication carrier containing proteins and nucleic acids, have been found in recent studies to play vital roles in directing the invasion and metastasis of tumor cells [53]. In general, EVs can be differentiated into four major categories: microvesicles (MV), exosomes, apoptotic bodies, and argosomes, which have different contents, functions, and sizes. In particular, the MVs and exosomes inside the tumor microenvironments contribute to most cancer-related intercellular events, and are accordingly known as tumor-associated EVs [54]. MVs have a typical diameter up to 1000 nm [55], and the diameters of exosomes normally range from 30 nm to 300 nm. MVs and exosomes are released by tumor cells and apoptotic cells into the tumor

microenvironment and interact with tumor stroma to promote a tumor-promoting environment. According to Figure 4.1 [56], the functions of EVs include CAF transformation, tumor cell communication, stimulation of endothelial cell growth (angiogenesis), and immune cell suppression. In fact, it has been revealed that EVs are present in potential tumor invasion areas ahead of any noticeable structural and molecular changes [5]. Therefore, the study of EVs offers the potential to significantly contribute to the understanding of tumor invasion mechanisms in unique ways. For clinical translation, the leading occurrence of EVs in potential tumor invading areas makes these a prospective cancer biomarker that can predict cancer invasion and assess the microenvironment in more accurate and more effective ways.

Various kinds of detection methods for EVs have emerged recently, such as flow cytometry performed on circulating exosomes to detect early pancreatic cancer [57], and immune-based detection [58]. Specifically, direct visualization of EVs in cellular environments is a highly valued approach to discover more of their properties including sizes, chemical content, spatial distribution, and

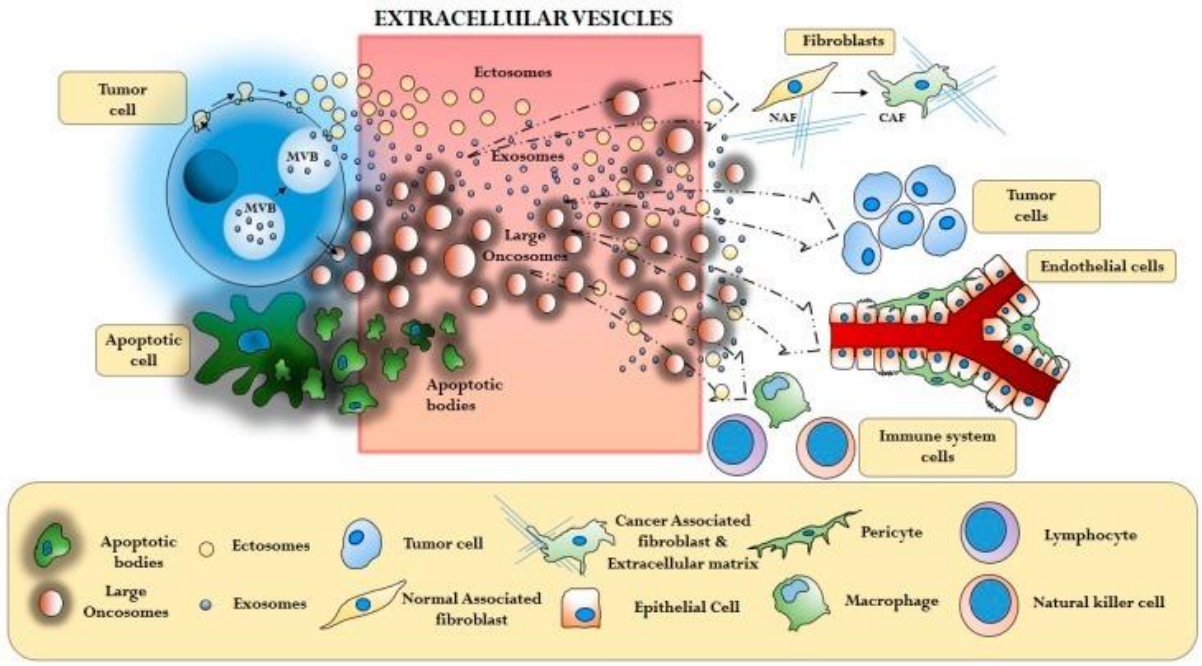

Figure 4.1 Extracellular vesicles (EVs) mediate interaction between cancer cells and different components in the tumor microenvironment (CAF: cancer associated fibroblasts, ECM: extracellular matrix, MVB: multivesicular bodies, NAF: normal tissue associated fibroblasts) [56].

dynamics. Labeled imaging of EVs, realized by deliberate fluorescent labeling strategies, have observed the secretion of EVs by cells and their following dynamics [59]. However, as discussed in that study, there are many strict criteria for labeling designs in EV studies, many of which cannot always be met in certain circumstances, especially for *in vivo* human tissues.

A label-free approach for imaging EVs was investigated with the use of a multimodal nonlinear optical imaging and Raman spectroscopy [5]. Co-registered multi-contrast images of EVs and other tumor tissue features revealed that EVs begin to spread into benign tissues before any macroscopic events like ECM reorganization occur [5]. However, this study only used an animal model, primarily because of the challenges to access fresh and unperturbed human breast tumor tissues excised from breast cancer surgery. By integrating four major nonlinear optical imaging modalities into a portable cart for a label-free EV study, it is now possible to image untreated human tissue in the operating room immediately after surgical tissue excision, which enables a more accurate representation of the dynamic structural and molecular changes that are occurring within a tumor and its surrounding microenvironment.

4.2 Visualization and quantification of EV

Because of their membranes, most EVs, especially MVs, can be visualized by THG imaging through good phase-matching conditions. A former lab-based label-free EV imaging study also utilized 3PF and 2PF to provide further EV information [5]. However, because of the non-ideal laser source used in this intraoperative imaging system, 2PF and 3PF imaging modalities were not sensitive enough to effectively visualize the EVs. Therefore, THG was the only imaging modality used for the intraoperative characterization of EVs.

An example of EV imaging is shown in the THG-contrast image in Figure 4.2 (B) with highlighted interface structures such as the boundaries of adipocytes. In particular, there are many bright and point-like dots identified in this THG-contrast image, which are recognized as EVs. A simple EV segmentation algorithm was developed to quantify EV count (Figure 4.2 (A)). By applying this algorithm on images such as shown in Figure 4.2 (B), the generated binary image highlights the presence of EVs, as

shown in Figure 4.2 (C). The image intensity was inverted in this image for a better presentation.

To validate this imaging method of EV quantification, THG-contrast images were acquired for purified EVs isolated from human cancer cell lines with a known, labeled concentration of 3×10^{10} mL^{-1} measured by a standardized technique and commercial instrument – Nanosight (NS300, Nanosight, Ltd.). This Nanosight instrument utilizes a Nanoparticle Tracking Analysis (NTA) approach that is based on analyzing the properties of both light scattering and Brownian motion to obtain the particle size distribution of samples in a liquid suspension [60]. An example of a THG-contrast image of purified EVs is presented in Figure 4.2 (D) with the corresponding binary image in Figure 4.2 (E) processed by using the segmentation algorithm illustrated in Figure 4.2 (A). Notably, the threshold intensity I_{th} in Figure 4.2 (A) was empirically defined as the signal intensity at a certain percentage of pixel intensity from the histogram of each image. This percentage was deliberately determined based on the segmentation performance for faithfully highlighting the presence of EVs and for suppressing background structures

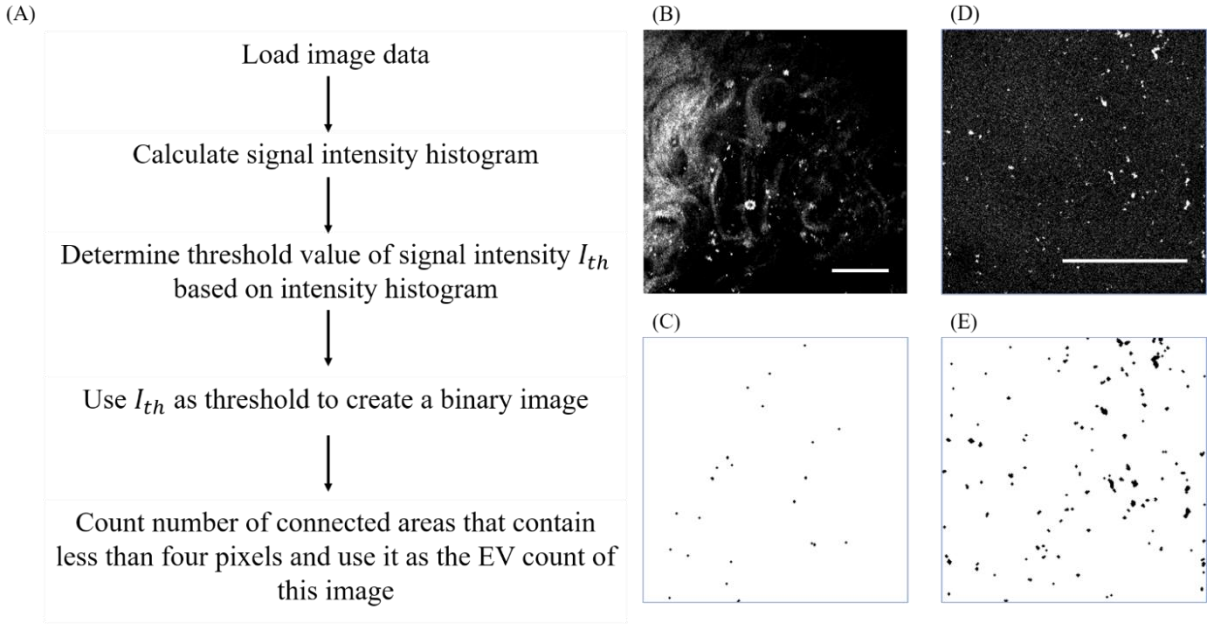

Figure 4.2 Quantification of EV information contained in THG-contrast images. (A) Flow of the EV quantification algorithm. (B) Original THG-contrast image of a purified EV solution. (C) Binary image showing segmented EVs (black dots) converted from the THG-contrast image of a purified EV solution using the algorithm shown in (A). (D) Original THG-contrast image of *ex-vivo* human breast cancer tissue collected in operating room. (E) Binary image of segmented EVs (black dots) converted from image (D) using the algorithm shown in (A). Scale bar: 100 µm.

and other noise, and was kept the same for all THG-contrast images of EVs. Considering the axial resolution and FOV characterized in Section 2.4, the 3D imaging volume of each THG-contrast image of EVs is calculated to be 100 μm×100 μm×1 μm = 10^{-8} mL. The EVs quantified from five images with the same imaging volume using the segmentation algorithm in Figure 4.2 (A) yielded an average count with standard deviation of 105 ± 12.3 per image volume that gives an approximate EV concentration of 1×10^{10} mL^{-1}. Reassuringly, the EV concentration quantified using these THG-contrast images and the segmentation algorithm is of the same magnitude as the labeled concentration measured by the commercial Nanosight instrument. Therefore, the EV counts per FOV quantified from the intraoperative THG-contrast images convincingly represent the real distribution of EVs in the tumor microenvironment.

4.3 Differentiation of breast tissue types using EV count

Figure 4.3 highlights the clear difference between EV count per FOV quantified from the THG-contrast images of cancerous tissues from breast cancer cases versus those of healthy tissues from breast reduction cases. Each bar in Figure 4.3 represents an individual case. Because only one THG-contrast

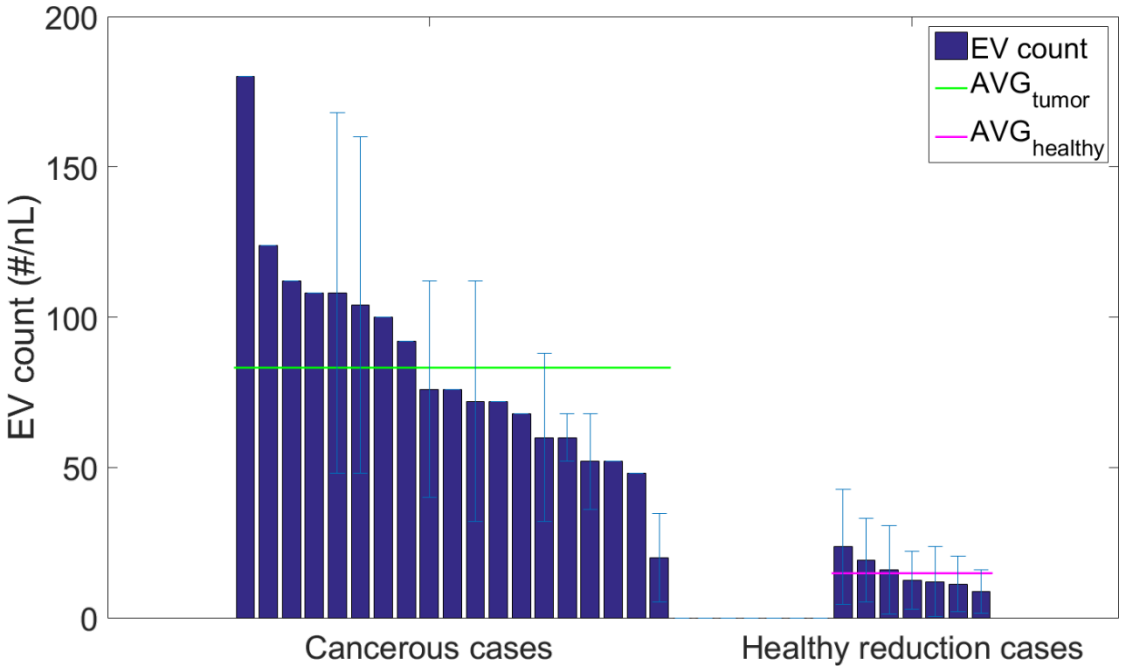

Figure 4.3 Quantification of EV count for breast cancer cases and healthy breast reduction cases. Green and pink lines mark the average EV count per nanoliter (nL) for cancerous cases and healthy breast reduction cases, respectively.

image was collected for these cases due to the limited image acquisition time restrained by surgical work flow, some of the bars for the breast cancer cases do not have an error bar. Average EV count is around 83/nanoliter (nL) for cancerous cases, and 15/nL for healthy breast reduction cases. This substantial difference correlates well with the fact that tumor tissues are generally more metabolically active than healthy tissue, and also because a larger number of EVs are produced by tumor cells as messengers to promote various tumor-promoting or preconditioning processes such as angiogenesis [56]. Therefore, the quantified EV count per FOV represents a good indicator of tissue types (cancerous / healthy).

4.4 Fitting of EV count versus distance to closest margin

Good correlations were also found between EV count and pathological tissue diagnosis. First, it was noted that there were 7 out of 19 breast cancer cases that shared similar pathological results, such as the same invasiveness grade for both IDC and DCIS. Among these cases, EV counts from each image were correlated with the corresponding distance from the IDC or DCIS to the most adjacent margin. As expected, there was a decreasing trend of EV count with increasing distance from the IDC or DCIS. These curves were fitted with decreasing exponentials (Figure 4.4) having R-squared values of 0.86 and

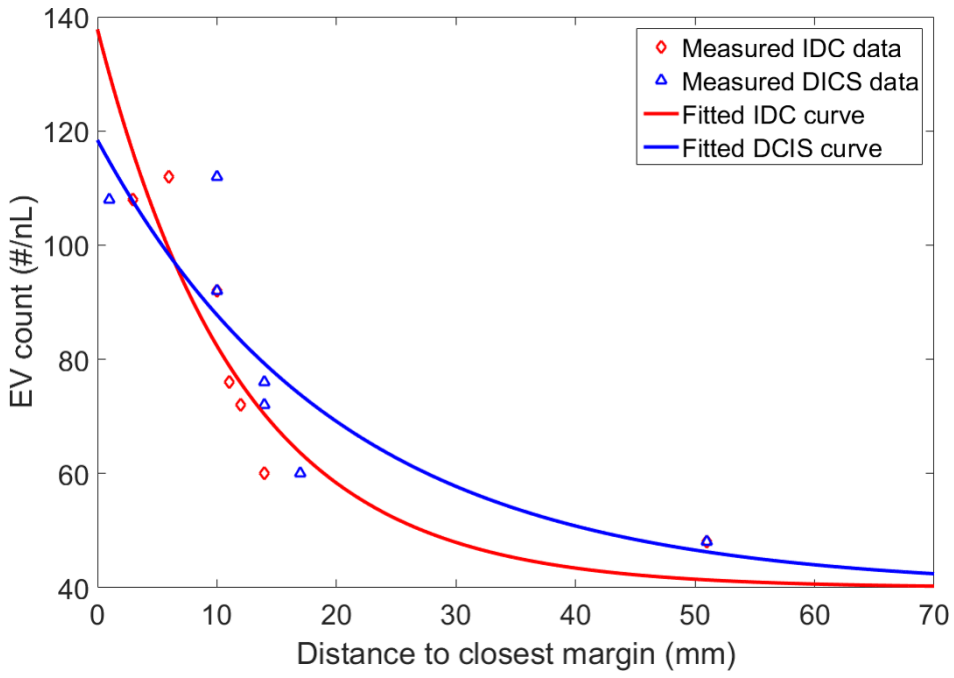

Figure 4.4 Exponential fitting results of EV count versus distance to closest IDC or DCIS tumor margin.

0.74 for the fitted IDC and DCIS distance curves, respectively. Considering the IDC curve as an example, the fitted EV count per FOV $S(d)$ was expressed as a function of the closest margin distance d

$$S(\mathrm{d}) = A\exp(B\,\mathrm{d}) + C \tag{4.1}$$

where $C = 40$ is the imaging offset, and $B = -0.0837$ represents the attenuation coefficient of EV count upon traveling a given distance within the tumor microenvironment. While the imaging offset C describes the noise and artifacts of the THG-contrast images, and attenuation coefficient B depends on the material properties of the breast tissue, the factor $A = 98$ before the exponential term is related to the invasiveness of breast cancer, which is independent of the distance from the IDC/DCIS to the closest margin. In this study, this factor was termed as an "invasiveness indicator", which is significant when correlating EV information with tumor invasiveness.

4.5 Correlation of tumor invasiveness with EV count

Unlike the correlation of EV count per FOV with distance to the closest tumor margin, there were not as many cases with the same or similar closest margin distance to explore for correlations with cancer invasiveness grade of IDC and DCIS. Instead, the fitting parameter termed as the "invasiveness indicator" in the previous section was used to evaluate cancer invasiveness.

Assuming the imaging offset and attenuation coefficient are the same for the THG-contrast images collected from other breast cancer cases with different invasiveness grades of IDC and DCIS, the invasive indicators A were calculated by substituting the closest tumor-margin distance and average EV count per FOV of each case into the fitting function in Eqn. (4.1) with the fixed fitting parameters $B = -0.0837$ and $C = 40$. By doing so, the invasiveness of different breast cancer cases characterized by EV count could be directly compared regardless of the different tumor-margin distances. Correlations of the invasiveness indicator with IDC and DCIS grades are shown in Figure 4.5 (A) and Figure 4.5 (B). The trend of IDC invasiveness indicator correlates well with the IDC invasiveness grade obtained from the pathology reports. However, the invasiveness indicators of DCIS were found to be roughly the same for DCIS invasiveness grade I and grade II, and a remarkable indicator increase appears at grade III.

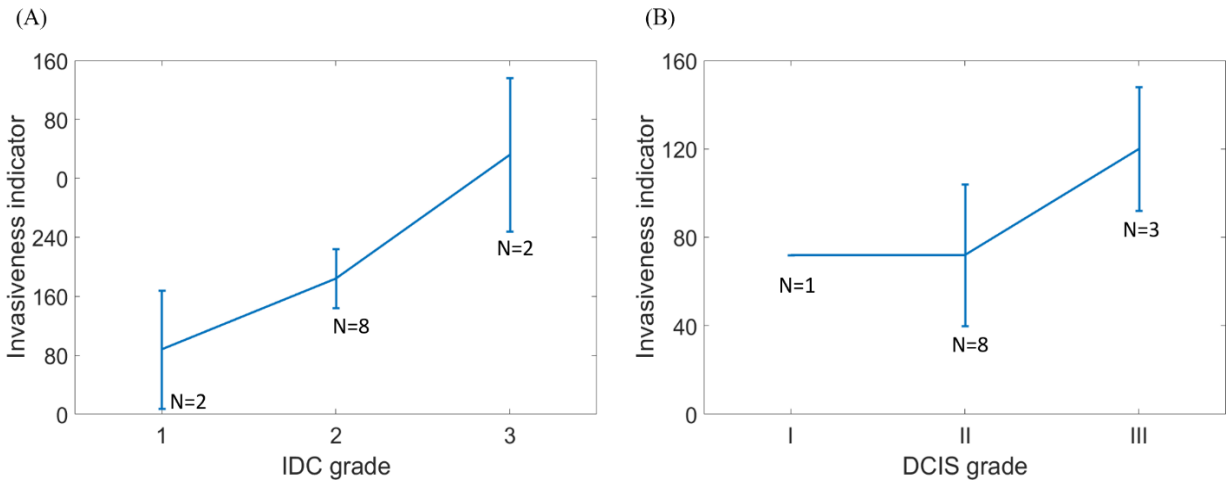

Figure 4.5 Correlation of invasive indicator with invasiveness grade of (A) IDC and (B) DCIS.

4.6 Summary

To summarize, EVs were visualized in THG-contrast images using the intraoperative imaging system, and quantified by a straightforward segmentation algorithm. Experiments on purified EVs validated the ability of the THG imaging modality to faithfully visualize EVs, and established the quantified EV counts per unit volume in the intraoperative images to be a good indicator of the real EV concentrations/densities.

Utilizing the quantified EV count per unit volume, correlations were found with the pathological characteristics of each case imaged. The most straightforward correlation was found for discriminating cancerous versus healthy tissues by EV counts. Furthermore, an exponential decay curve was fitted with the EV counts of several breast cancer cases with different distances to closest margin controlling for the same invasiveness grade. Utilizing the fitting results, the EV information was correlated with the invasiveness grades of IDC and DCIS.

The overall trends of EV correlations with pathological characteristics present a promising way of examining cancer invasion by quantifying EV counts from the THG-contrast images, which can be clinically translated to acquire larger numbers of cases, specimens, and images in the future.

5 Conclusions and future directions

This thesis reports the development of an intraoperative and label-free approach to visualize human breast tumor microenvironments, particularly EVs, which serve as cancer-promoting messengers. Based on the label-free multimodal nonlinear optical imaging demonstrated in the lab [4, 5], this work acts as the first step for translating the lab-developed nonlinear optical imaging technology into clinical applications. By shifting the imaging system from the laboratory to the operating room, fresh untreated human tumor tissue became more accessible to image and investigate, and essential information of the tumor microenvironment like EV count was obtained with high accuracy and sensitivity. Equipped with four nonlinear optical imaging modalities, multiple intrinsic structural and molecular contrasts of breast tissues were excited and detected, providing combinatorial characterization of tissue structures and chemical components, such as cells, fibrous structures, and adipocyte. Acquired multi-contrast image datasets contained extra contrasts compared to standard H&E stained histology, and were acquired with much less time and labor. These unique capabilities and advantages of the intraoperative multimodal nonlinear optical imaging system make it a promising method of assessing the excised breast tumor microenvironments for pathological investigations.

The conditions in the operating room imposed special requirements for designing and building this intraoperative imaging system, including its compact size, robust operation, light concealment, and laser safety. The optical and mechanical components were deliberately chosen to meet these requirements for intraoperative imaging. However, several compromises were made to balance the imaging performance and the intraoperative imaging requirements. The powerful pulse shaper-enhanced PCF source used in a lab-based system [6] was substituted with a narrow band femtosecond laser that is significantly more compact and robust. In this case, excitation efficiency was compromised for the compact integration and robust operation. For the same reason, sequential detection of the nonlinear signals by a single PMT was implemented instead of using simultaneous detection of the four channels by multiple PMTs [6], which resulted in a much slower image acquisition speed. Nonetheless, these

compromises were worthwhile considering the significant amount of multi-contrast nonlinear optical images acquired from fresh untreated human breast tissue, which are usually inaccessible and unavailable for lab-based imaging.

Before characterizing the visualized tumor microenvironment, the imaging characteristics of the system including lateral and axial resolution, FOV, and imaging speed were tested using resolution and grid targets and fluorescent beads. Experimental results matched well with theoretical calculations. Using these imaging characteristics, the scale of tissue structures in multi-contrast nonlinear optical images was determined, and thus tissue features were recognized from the multi-contrast nonlinear optical images and then characterized by comparing with the co-located histology at the same scale. Basic structures like adipocytes, fibrous structures, and different types of cells were characterized with good correlations found with histology. These served as building blocks for more complicated structures and events in the breast tissues that are important for pathological diagnosis. By imaging various breast tumor tissues, this system revealed its potential ability for differentiating tumor subtypes and recognizing subtle events and reactions. In the future, it is likely that multimodal nonlinear optical imaging will function as a real-time imaging tool for routine biopsy to reduce the cost and to relieve patient anxiety caused by long wait times.

As an essential yet poorly understood tissue element, EVs were visualized in the THG-contrast images by the intraoperative imaging system and were quantified by a segmentation algorithm. Feasibility and credibility tests using a purified EV solution revealed similar EV concentrations measured by both the THG imaging and a state-of-art commercial system and technique provided by the Nanosight instrument, which helped validate THG imaging as a reliable and convincing tool to visualize EVs in the *ex vivo* human breast tissue specimens. Through applying the same quantification algorithm on every THG-contrast image, an EV count per FOV was recorded for each image, and an average EV count was calculated for each case. Pathology reports provided important pathological information like cancer invasiveness grade and the distance from the imaged site on the surgical margin to the closest tumor margin. To prove the significance of EVs in tumor invasion, efforts were made to find correlations between EV count and pathological characteristics. First, EV counts were found to be higher in cancerous

breast tissues from breast cancer cases than in healthy breast tissues from breast reduction surgeries, corroborating the fact that tumor cells are major producers of EVs in human breast cancer. Furthermore, exponential fitting was used to represent the change in EV count per unit volume with increasing distance from the tumor margin, controlling for other variables, demonstrating the attenuation of EV count with increasing distance from the tumor. Finally, utilizing these fitting results, cases with different invasiveness grades were compared by their invasiveness indicator, one of the fitting parameters based on the EV counts and margin distance. As expected, the invasiveness indicator calculated by the EV count fitting increased with increasing invasiveness grade.

Since this imaging system is the first attempt at clinical translation of label-free multimodal nonlinear optical imaging, there are various improvements to be done in the future. The most straightforward work will be the implementation of an optimal laser source that is comparable to that used in previous lab-based studies for better imaging performance. Unfortunately, there are no commercial laser sources available that generate the same spectral range as the optimal source for label-free nonlinear optical imaging. However, there are solutions to reduce the size of the pulse shaper and PCF, and to stabilize them as well. For example, a motorized stage can retain the position of PCF alignment. In this sense, the same laser source can be integrated into a portable cart to achieve higher excitation efficiency. In addition, the current imaging cart was not customized, and it had a limited capacity (3'×3'×4') of housing more optical components and a moderate net weight that facilitated the moving and operating of the imaging cart by single person. A customized cart designed to take into consideration the intraoperative requirements as well as the setup of the nonlinear optical imaging hardware will potentially increase the capacity and maintain a compact size and an appropriate weight to maintain good portability. Then, in this more spacious cart, simultaneous detection and imaging mosaics can be realized by using multiple PMTs and a motorized translational stage, which, when combined with the more optimal laser source, will provide a much faster imaging speed, a larger FOV, and the ability to easily locate imaging sites on tissue. Intraoperative assessment of tumor margins in lumpectomy cases will be possible with the fully customized intraoperative imaging cart. The larger data volume collected from cases will also realize a

more comprehensive characterization of the tumor microenvironment.

As for EV quantification, the more significant limitation was the number of cases effectively imaged and analyzed. In most cases involving a mastectomy, the collected images were from pure adipose tissue, which did not provide much useful information because of the low number of EVs. However, using a higher imaging speed and greater control of imaging sites, the surrounding tumor microenvironment could be evaluated more efficiently, and more sets of multi-contrast images could be acquired for each case, which will also improve the statistical significance of these results. In addition, an improved diffusion model for characterizing the EV distribution for distances away from the tumor margin could be established to study the physical mechanisms of EV transportation and biodistribution in human breast tumor tissues.

This portable label-free multimodal nonlinear optical imaging system was built to intraoperatively image the breast tumor microenvironment. The correlations with co-located histology validated the ability of this system to visualize basic tissue structures, recognize and differentiate breast tumor subtypes, and highlight subtle tissue events. In particular, this imaging system was the first to intraoperatively visualize the important subcellular structure – EVs, in the *ex vivo* tumor microenvironment. The quantification of EVs from the label-free nonlinear optical images revealed good correlations with the pathological diagnosis. Moreover, future modifications to this system could greatly improve the imaging performance such as the acquisition speed, the FOV, and the excitation efficiency. These improvements will enable a more global examination of the breast tumor tissue specimens and quantification of EVs with greater statistical significance. With these improvements, the imaging system could be used for intraoperative stain-free histopathology, to develop EVs as a biomarker for evaluating the invasiveness of a breast tumor, and for assessing tumor margins in a more quantified and accurate way.

References

[1] I. Kaminer, J. Nemirovsky and M. Segev, "Optimizing 3D multiphoton fluorescence microscopy," *Opt. Lett.*, vol. 38, no. 19, pp. 3945–3948, 2013.

[2] S. Huang, A. A. Heikal and W. W. Webb, "Two-photon fluorescence spectroscopy and microscopy of NAD(P)H and flavoprotein," *Biophys. J.*, vol. 82, no. 5, pp. 2811–2825, 2002.

[3] X. Chen, O. Nadiarynkh, S. Plotnikov and P. J. Campagnola, "Second harmonic generation microscopy for quantitative analysis of collagen fibrillar structure," *Nat. Protoc.*, vol. 7, no. 4, pp. 654–669, 2012.

[4] H. Tu, Y. Liu, D. Turchinovich, M. Marjanovic, J. K. Lyngsø, J. Lægsgaard, E. J. Chaney, Y. Zhao, S. You, W. L. Wilson, B. Xu, M. Dantus and S. A. Boppart, "Stain-free histopathology by programmable supercontinuum pulses," *Nat. Photonics*, vol. 10, no. 8, pp. 534–540, 2016.

[5] H. Tu, Y. Liu, M. Marjanovic, E. J. Chaney, S. You, Y. Zhao and S. A. Boppart, "Concurrence of extracellular vesicle enrichment and metabolic switch visualized label-free in the tumor microenvironment," *Sci. Adv.*, vol. 3, no. 1, p. e1600675, 2017.

[6] S. You, H. Tu, E. J. Chaney, Y. Sun, Y. Zhao, A. J. Bower, Y. Liu, M. Marjanovic, S. Sinha, Y. Pu and S. A. Boppart, "Intravital imaging by simultaneous label-free autofluorescence-multiharmonic (SLAM) microscopy," *Nat. Commun.*, Under review, 2017.

[7] D. A. Orringer, B. Pandian, Y. S. Niknafs, T. C. Hollon, J. Boyle, S. Lewis, M. Garrard, S. L. Hervey-Jumper, H. J. L. Garton, C. O. Maher, J. A. Heth, O. Sagher, D. A. Wilkinson, M. Snuderl, S. Venneti, S. H. Ramkissoon, K. A. McFadden, A. Fisher-Hubbard, A. P. Lieberman, T. D. Johnson, X. S. Xie, J. K. Trautman, C. W. Freudiger and S. Camelo-Piragua, "Rapid intraoperative histology of unprocessed surgical specimens via fibre-laser-based stimulated Raman scattering microscopy," *Nat. Biomed. Eng.*, vol. 1, no. 2, p. 27, 2017.

[8] Y. K. Tao, D. Shen, Y. Sheikine, O. O. Ahsen, H. H. Wang, D. B. Schmolze, N. B. Johnson, J. S. Brooker, A. E. Cable, J. L. Connolly and J. G. Fujimoto, "Assessment of breast pathologies using nonlinear microscopy," *Proc. Natl. Acad. Sci.*, vol. 111, no. 43, pp. 15304–15309, 2014.

[9] P. A. Franken, A. E. Hill, C. W. Peters and G. Weinreich, "Generation of optical harmonics," *Phys. Rev. Lett.*, vol. 7, no. 4, pp. 118–119, 1961.

[10] P. Stoller, P. M. Celliers, K. M. Reiser and A. M. Rubenchik, "Quantitative second-harmonic generation microscopy in collagen," *Appl. Opt.*, vol. 42, no. 25, pp. 5209–5219, 2003.

[11] P. P. Provenzano, D. R. Inman, K. W. Eliceiri, J. G. Knittel, L. Yan, C. T. Rueden, J. G. White and P. J. Keely, "Collagen density promotes mammary tumor initiation and progression," *BMC Med.*, vol. 6, no. 1, p. 11, 2008.

[12] R. W. Boyd, "Wave-equation description of nonlinear optical interactions," in *Nonlinear Optics*, Elsevier, pp. 67–127, 2003.

[13] Y. Barad, H. Eisenberg, M. Horowitz and Y. Silberberg, "Nonlinear scanning laser microscopy by third harmonic generation," *Appl. Phys. Lett.*, vol. 70, no. 8, pp. 922–924, 1997.

[14] T. Y. F. Tsang, "Optical third-harmonic generation at interfaces," *Phys. Rev. A*, vol. 52, no. 5, pp. 4116–4125, 1995.

[15] D. Débarre, W. Supatto, A.-M. Pena, A. Fabre, T. Tordjmann, L. Combettes, M.-C. Schanne-Klein and E. Beaurepaire, "Imaging lipid bodies in cells and tissues using third-harmonic generation microscopy," *Nat. Methods*, vol. 3, no. 1, pp. 47–53, 2006.

[16] D. Li, W. Zheng and J. Y. Qu, "Two-photon autofluorescence microscopy of multicolor excitation," *Opt. Lett.*, vol. 34, no. 2, pp. 202–204, 2009.

[17] G. H. Patterson and D. W. Piston, “Photobleaching in two-photon excitation microscopy,” *Biophys. J.*, vol. 78, no. 4, pp. 2159–2162, 2000.

[18] R. del Coso and J. Solis, “Relation between nonlinear refractive index and third-order susceptibility in absorbing media,” *J. Opt. Soc. Am. B*, vol. 21, no. 3, pp. 640-644, 2004.

[19] V. Besse, H. Leblond and G. Boudebs, “Fifth-order nonlinear susceptibility: Effect of third-order resonances in a classical theory,” *Phys. Rev. A - At. Mol. Opt. Phys.*, vol. 92, no. 1, pp. 1–10, 2015.

[20] K. P. Quinn, G. V Sridharan, R. S. Hayden, D. L. Kaplan, K. Lee and I. Georgakoudi, “Quantitative metabolic imaging using endogenous fluorescence to detect stem cell differentiation,” *Sci. Rep.*, vol. 3, p. 3432, 2013.

[21] W. R. Zipfel, R. M. Williams, R. Christie, A. Y. Nikitin, B. T. Hyman and W. W. Webb, “Live tissue intrinsic emission microscopy using multiphoton-excited native fluorescence and second harmonic generation,” *Proc. Natl. Acad. Sci.*, vol. 100, no. 12, pp. 7075–7080, 2003.

[22] D. M. Huland, K. Charan, D. G. Ouzounov, J. S. Jones, N. Nishimura and C. Xu, “Three-photon excited fluorescence imaging of unstained tissue using a GRIN lens endoscope,” *Biomed. Opt. Express*, vol. 4, no. 5, pp. 652-658, 2013.

[23] N. G. Horton, K. Wang, D. Kobat, C. G. Clark, F. W. Wise, C. B. Schaffer and C. Xu, “In vivo three-photon microscopy of subcortical structures within an intact mouse brain,” *Nat Phot.*, vol. 7, no. 3, pp. 205–209, 2013.

[24] Coherent Incorporation, web page. Available at https://www.coherent.com/lasers/laser/industrial-short-pulse-lasers/fidelity-femtosecond-fiber-lasers/fidelity-2-ultrafast-fiber-oscillator/. Accessesd October 2017.

[25] D. C. Sordillo, L. A. Sordillo, P. P. Sordillo and R. R. Alfano, "Fourth near-infrared optical window for assessment of bone and other tissues," *J. Biomed. Opt.*, vol. 9689, p. 96894J, 2016.

[26] Y. Pu, W. Wang, G. Tang and R. R. Alfano, "Changes of collagen and nicotinamide adenine dinucleotide in human cancerous and normal prostate tissues studied using native fluorescence spectroscopy with selective excitation wavelength," *J. Biomed. Opt.*, vol. 15, no. 4, p. 47008, 2010.

[27] American National Standards Institute, "American National Standard for safe use of lasers," Z136.1, 2014.

[28] N. Ramanujam, "Fluorescence spectroscopy of neoplastic and non-neoplastic tissues," *Neoplasia*, vol. 2, no. 1–2, pp. 89–117, 2000.

[29] C. Li, R. K. Pastila, C. Pitsillides, J. M. Runnels, M. Puoris'haag, D. Côté and C. P. Lin, "Imaging leukocyte trafficking *in vivo* with two-photon-excited endogenous tryptophan fluorescence," *Opt. Express*, vol. 18, no. 2, pp. 988-999, 2010.

[30] Olympus, Web page. Available at : https://www.olympus-lifescience.com/en/objectives/xlumplfln-w/. Accessed October 2017.

[31] W. R. Zipfel, R. M. Williams and W. W. Webb, "Nonlinear magic: multiphoton microscopy in the biosciences," *Nat. Biotechnol.*, vol. 21, no. 11, pp. 1369–1377, 2003.

[32] M. Gu, "Resolution in three-photon fluorescence scanning microscopy," *Opt. Lett.*, vol. 21, no. 13, pp. 988-990, 1996.

[33] N. Tian, L. Fu and M. Gu, "Resolution and contrast enhancement of subtractive second harmonic generation microscopy with a circularly polarized vortex beam," *Sci. Rep.*, vol. 5, p. 13508, 2015.

[34] V. Pavithra, S. Sowmya, R. S. Rao, S. Patil, D. Augustine, V. C. Haragannavar and S. Nambiar, "Tumor-associated collagen signatures: an insight," *World J. Dent.*, vol. 8, no. 3, pp. 224–330, 2017.

[35] R. Ambekar, T.-Y. Lau, M. Walsh, R. Bhargava and K. C. J. Toussaint, "Quantifying collagen structure in breast biopsies using second-harmonic generation imaging," *Biomed. Opt. Express*, vol. 3, no. 9, pp. 2021–2035, 2012.

[36] P. Campagnola, "Second harmonic generation imaging microscopy: Applications to diseases diagnostics," *Anal. Chem.*, vol. 83, no. 9, pp. 3224–3231, 2011.

[37] R. LaComb, O. Nadiarnykh, S. S. Townsend and P. J. Campagnola, "Phase matching considerations in second harmonic generation from tissues: Effects on emission directionality, conversion efficiency and observed morphology," *Opt. Commun.*, vol. 281, no. 7, pp. 1823–1832, 2008.

[38] H. Gray, "Subcutaneous tissue from a young rabit. Highly magnified," in *Anatomy of the Human body*, Lea and Febiger, p. 377, 1918.

[39] S. Halls, web page. Available at: http://breast-cancer.ca/idc/. Accessed November 2017.

[40] A. E. M. Reed, J. R. Kutasovic, S. R. Lakhani and P. T. Simpson, "Invasive lobular carcinoma of the breast: morphology, biomarkers and 'omics," *Breast Cancer Res.*, vol. 17, no. 1, p. 12, 2015.

[41] S. Luna-Moré, B. Gonzalez, C. Acedo, I. Rodrigo and C. Luna, "Invasive micropapillary carcinoma of the breast," *Pathol. - Res. Pract.*, vol. 190, no. 7, pp. 668–674, 1994.

[42] L. Bochet, C. Lehuédé, S. Dauvillier, Y. Y. Wang, B. Dirat, V. Laurent, C. Dray, R. Guiet, I. Maridonneau-Parini, S. Le Gonidec, B. Couderc, G. Escourrou, P. Valet and C. Muller, "Adipocyte-derived fibroblasts promote tumor progression and contribute to the desmoplastic reaction in breast cancer," *Cancer Res.*, vol. 73, no. 18, pp. 5657–5668, 2013.

[43] H. Kim, J. Watkinson, V. Varadan and D. Anastassiou, "Multi-cancer computational analysis reveals invasion-associated variant of desmoplastic reaction involving INHBA, THBS2 and COL11A1," *BMC Med. Genomics*, vol. 3, no. 1, p. 51, 2010.

[44] C. A. Iacobuzio-Donahue, P. Argani, P. M. Hempen, J. Jones and S. E. Kern, "The desmoplastic response to infiltrating breast carcinoma: Gene expression at the site of primary invasion and implications for comparisons between tumor types," *Cancer Res.*, vol. 62, no. 18, pp. 5351–5357, 2002.

[45] M. A. Troester, M. H. Lee, M. Carter, C. Fan, D. W. Cowan, E. R. Perez, J. R. Pirone, C. M. Perou, D. J. Jerry and S. S. Schneider, "Activation of Host Wound Responses in Breast Cancer Microenvironment," *Clin. Cancer Res.*, vol. 15, no. 1522, pp. 7020–7028, 2009.

[46] H. Ohtani, "Stromal reaction in cancer tissue: pathophysiologic significance of the expression of matrix-degrading enzymes in relation to matrix turnover and immune/inflammatory reactions," *Pathol. Int.*, vol. 48, no. 1, pp. 1–9, 1998.

[47] M. W. Conklin and P. J. Keely, "Why the stroma matters in breast cancer: Insights into breast cancer patient outcomes through the examination of stromal biomarkers," *Cell Adhes. Migr.*, vol. 6, no. 3, pp. 249–260, 2012.

[48] C. A. Wells and G. A. El-Ayat, "Non-operative breast pathology: apocrine lesions," *J. Clin. Pathol.*, vol. 60, no. 12, pp. 1313–1320, 2007.

[49] J. K. Warner, D. Kumar and W. A. Berg, “Apocrine metaplasia: mammographic and sonographic appearances,” *AJR. Am. J. Roentgenol.*, vol. 170, no. 5, pp. 1375–1379, 1998.

[50] A. C. Kushwaha, M. O’Toole, N. Sneige, C. B. Stelling and M. J. Dryden, “Mammographic—pathologic correlation of apocrine metaplasia diagnosed using vacuum-assisted stereotactic core-needle biopsy: our 4-year experience,” *Am. J. Roentgenol.*, vol. 180, no. 3, pp. 795–798, 2003.

[51] R. J. Brenner, R. J. Jackman, S. H. Parker, W. P. Evans, L. Philpotts, B. M. Deutch, M. C. Lechner, D. Lehrer, P. Sylvan, R. Hunt, S. J. Adler and N. Forcier, “Percutaneous core needle biopsy of radial scars of the breast: When is excision necessary?” *Am. J. Roentgenol.*, vol. 179, no. 5, pp. 1179–1184, 2002.

[52] C. Morgan, Z. A. Shah, R. Hamilton, J. Wang, J. Spigel, W. Deleon, P. Deleon, T. Leete and J. M. Fulmer, “The radial scar of the breast diagnosed at core needle biopsy,” *Proc. (Bayl. Univ. Med. Cent.)*, vol. 25, no. 1, pp. 3–5, 2012.

[53] V. Muralidharan-Chari, J. W. Clancy, A. Sedgwick and C. D’Souza-Schorey, “Microvesicles: mediators of extracellular communication during cancer progression,” *J. Cell Sci.*, vol. 123, no. 10, pp. 1603–1611, 2010.

[54] F. T. Borges, L. A. Reis and N. Schor, “Extracellular vesicles: structure, function, and potential clinical uses in renal diseases,” *Brazilian J. Med. Biol. Res.*, vol. 46, no. 10, pp. 824–830, 2013.

[55] G. Raposo and W. Stoorvogel, “Extracellular vesicles: exosomes, microvesicles, and friends,” *J. Cell Biol.*, vol. 200, no. 4, pp. 373–83, 2013.

[56] C. Ciardiello, L. Cavallini, C. Spinelli, J. Yang, M. Reis-Sobreiro, P. De Candia, V. R. Minciacchi and D. Di Vizio, “Focus on extracellular vesicles: New frontiers of cell-to-cell communication in cancer,” *Int. J. Mol. Sci.*, vol. 17, no. 2, pp. 1–17, 2016.

[57] S. A. Melo, L. B. Luecke, C. Kahlert, A. F. Fernandez, S. T. Gammon, J. Kaye, V. S. Lebleu, E. A. Mittendorf, J. Weitz, N. Rahbari, C. Reissfelder, C. Pilarsky, M. F. Fraga, D. Piwnica-worms and R. Kalluri, "Glypican-1 identifies cancer exosomes and detects early pancreatic cancer," *Nature*, vol. 523, no. 7559, pp. 177–182, 2015.

[58] D. Duijvesz, C. Y. L. Versluis, C. A. M. Van Der Fels, M. S. Vredenbregt-Van Den Berg, J. Leivo, M. T. Peltola, C. H. Bangma, K. S. I. Pettersson and G. Jenster, "Immuno-based detection of extracellular vesicles in urine as diagnostic marker for prostate cancer," *Int. J. Cancer*, vol. 137, no. 12, pp. 2869–2878, 2015.

[59] C. P. Lai, E. Y. Kim, C. E. Badr, R. Weissleder, T. R. Mempel, B. A. Tannous and X. O. Breakefield, "Visualization and tracking of tumour extracellular vesicle delivery and RNA translation using multiplexed reporters," *Nat. Commun.*, vol. 6, p. 7029, 2015.

[60] Nanosight, web page. Available at: https://www.malvern.com/en/products/product-range/nanosight-range/. Accessed November 2017.